Precambrian Research 321 (2019) 13–33

Contents lists available at ScienceDirect

Precambrian Research

journal homepage: www.elsevier.com/locate/precamres

Mineralogy, geochemistry, and zircon U-Pb-Hf isotopes of the Paleoproterozoic granulite-facies metamorphic rocks from the Aketashitage area, southeastern Tarim Craton

Zhong-Mei Wang[a,*], Chun-Ming Han[b,c], Wen-Jiao Xiao[a,c], Patrick Asamoah Sakyi[d], Lei Yang[a], Na Zhao[b]

[a] State Key Laboratory of Lithospheric Evolution, Institute of Geology and Geophysics, Chinese Academy of Sciences, Beijing 100029, China
[b] Key Laboratory of Mineral Resources, Institute of Geology and Geophysics, Chinese Academy of Sciences, Beijing 100029, China
[c] Xinjiang Research Center for Mineral Resources, Urumqi 830011, China
[d] Department of Earth Science, University of Ghana, P.O. Box LG 58, Legon-Accra, Ghana

ARTICLE INFO

Keywords:
Garnet-biotite gneiss
Mafic granulite
Zircon U-Pb ages and Hf isotopes
Dunhuang Block
Active continental margins

ABSTRACT

The key to understanding the generation of mantle-derived magma and the formation of new continental crust is the recognition of the granulite-facies metamorphism, associated partial melting, and coeval magmatism that are documented in active continental margins. We firstly present a combined analysis of petrography, mineral chemistry, zircon U-Pb ages and hafnium (Hf) isotopes, in addition to whole-rock geochemistry on the garnet-biotite gneisses (Grt-Bi gneisses) and mafic granulites from the Aketashitage area, southeastern Tarim Craton. The implications of this analysis are discussed with respect to the thermal and tectonic evolution of the Tarim Craton. The Grt-Bi gneisses and mafic granulites are strongly peraluminous in composition and have flat REE patterns with negative Eu anomalies that are identical to those from the middle crust but higher than lower continental crust. Both the Grt-Bi gneisses and the mafic granulites have negative Nb-Ta anomalies, slightly positive Zr-Hf anomalies, and pronounced positive spikes in U and Pb. The characteristics in whole-rock geochemistry and mineral compositions indicate that the Grt-Bi gneisses and mafic granulites have the same source locality, which is most likely the garnet-bearing middle crust. The retrograde metamorphic P-T estimates for the Grt-Bi gneisses and mafic granulites are T = 574 °C; P = 7.0 kbar and T = 715 °C; P = 7.0 kbar, respectively. SIMS zircon U-Pb dating results reveal a large spread in metamorphic ages (2036–1962 Ma) for these granulite-facies rocks, interpreted to be the consequence of a large amount of magmas being added to the crust in an uninterrupted manner. Zircon Hf isotopes are characterized by variable but mostly negative ε_{Hf} (t) values (−18.2 to −0.6), reasonably uniform Hf isotopic compositions, and highly variable T_{DM}^{C} model ages between 2628 and 3599 Ma, representing a long-lived reworking of the preexisting crust. Our data, along with available geological evidences, lead us to propose a model for the evolution of the Dunhuang Block in the Paleoproterozoic. That is, the southeastern margin of the Tarim Craton, the Dunhuang Block was possibly an active continental margin during the Paleoproterozoic. The steep subduction of oceanic slab resulted in the thickening of the continental crust, which in turn caused the crust anatexis. The increase in asthenosphere high heat flow and the intrusion of mantle-derived magma induced extensive heating, which preceded the granulite-facies metamorphism and coeval magmatism in the middle crust of the southern Tarim Craton.

1. Introduction

The typical accretionary orogeny is commonly characterized by high heat flow, granulite-facies metamorphism and associated partial melting, and coeval plutonism (Xiang et al., 2014). In general, these geologic processes are the diagnostic features of active continental margins, and potentially provide a window into understanding the generation of mantle-derived magma and the formation of new continental crust (Collins, 2002; Hyndman et al., 2005; Klepeis et al., 2007; Zhang et al., 2013b). Accordingly, knowledge of the origin and petrogenesis of the deep-seated magmatism and metamorphism in active continental margins is essential to evaluate continental building

* Corresponding author.
E-mail address: wangzm@mail.iggcas.ac.cn (Z.-M. Wang).

https://doi.org/10.1016/j.precamres.2018.11.003
Received 8 May 2018; Received in revised form 10 November 2018; Accepted 11 November 2018
Available online 13 November 2018
0301-9268/ © 2018 Elsevier B.V. All rights reserved.

processes (Debari, 1994; Jagoutz et al., 2007; Zhang et al., 2013b). The granulite-facies rocks exposed in high-grade regional metamorphic belts and exhumed as xenoliths in basaltic pipes are considered to be a window to decipher the properties of the lower crust, past and present (Harley, 1989; Wei, 2016; Mao et al., 2017). Granulite-facies metamorphic rocks are accessible either as large tracts of surface outcrop or as tiny fragments in deep volcanic conduits (Rudnick and Fountain, 1995). These granulite-facies rocks can not only provide constraints on understanding the probable nature and composition of the lower crust in the existing continents, but they also provide an insight into the interpretation of formation and reworking of the continental crust, as well as orogenic mechanisms. An exhaustive understanding of the tectonic settings, petrogenesis, and metamorphism of granulite-facies rocks provide an ability to better recognize the evolutionary history of the continental crust. It is clear that granulite-facies metamorphism may accompany, or very shortly follow, continental crust formation in some instances; whereas in other cases, it affects continental crust that was formed much earlier and has possibly been affected by intervening events (Bohlen and Mezger, 1989). Thus, a great number of systematic studies have been carried out to determine the formation environment and metamorphic evolution of these granulite-facies rocks (Bohlen and Mezger, 1989; Harley, 1989; Rudnick and Fountain, 1995; MÜNtener et al., 2000).

The Dunhuang Block, situated between the Tethyan domain, the Tarim Craton, the North China Craton and the Central Asian Orogenic Belt (CAOB) (Fig. 1), has been long considered to be part of the basement of the Tarim Craton or the western part of the Alxa Block of the North China Craton (Lu et al., 2008; Zhang et al., 2012, 2013a; He et al., 2013; Xu et al., 2013; Long et al., 2014). However, some researchers proposed that the Dunhuang Block was involved into the early Paleozoic orogeny, representing the southernmost margin of the CAOB (Zhao et al., 2015a, 2016). New found high-grade metamorphic rocks also reveal that the Dunhuang Block underwent Paleozoic subduction and/or collision events (Zong et al., 2012; He et al., 2014; Wang et al., 2016, 2017a). The above research principally focused on the Paleozoic high-grade metamorphic rocks exposed in the northeast segment of the Dunhuang Block (Fig. 2a), thus, our understanding of the evolutionary history of the Dunhuang Block is hampered by the scarcity of data relating to high-grade metamorphic rocks of different ages or those are exposed in other regions. This knowledge gap is mainly the result of the extensive cover of the Gobi Desert. This study focuses on the Paleoproterozoic Grt-Bi gneisses and mafic granulites in the Aketashitage area, Dunhuang Block, southern Tarim Craton (Fig. 2a and b), with a view to better understanding the early evolutionary history of the Tarim Craton in addition to the reconstruction of the tectonic framework prior to the onset of the orogeny. We present new petrographic evidence, as well as major and trace element mineral chemistry that documents garnet growth to place some constraints on identifying the high-grade metamorphism. SIMS U-Pb in situ zircon dating enables the timing of the metamorphic events that produced the garnet crystals to be defined. In addition, whole-rock geochemistry and zircon Hf isotopes are presented in order to explain the petrogenesis of their protoliths. All the presented data of these granulite-facies metamorphic rocks should be used to discuss their implications with respect to the thermal and tectonic evolution of the Tarim Craton. Our new data provides direct information that the Grt-Bi gneisses and mafic granulites in the Aketashitage area record a long-lived metamorphism. Combined with previously reported coeval magmatism and crust anatexis suggest that the Dunhuang Block, southeastern Tarim Craton, was possibly an active continental margin involved in the assembly of the Columbia supercontinent. Our results contribute to a better understanding of crustal growth and reworking in an active continental margin tectonic setting.

2. Geological background and sampling

The Dunhuang Block lies to the east of the Tarim Craton, to the south of the Beishan Orogen (the southern margin of the CAOB), to the north of the Altyn Tagh Fault (Fig. 1). Previously, the Dunhuang Block had been widely accepted as a part of the Precambrian cratonic block or microcontinent dominated by Precambrian crystalline basement rocks, which are defined as the Milan Complex in the northeastern Altyn Tagh area, and the Dunhuang Complex in the Dunhuang area (BGMRG, 1989; Mei et al., 1997, 1998; Xu et al., 1999; Lu et al., 2008; Zhang et al., 2011). However, the latest studies propose that it is more reasonable to regard the Dunhuang Block as an orogenic belt (Zhao et al., 2016, 2017; Wang et al., 2017b), and the exposed rocks are considered to be primarily composed of Archean-early Mesoproterozoic crystalline basement rocks, Paleozoic high-grade metamorphic rocks and Paleozoic magmatic rocks (Zhao et al., 2017).

The exposed Archean-early Mesoproterozoic rocks in the Dunhuang Block are mainly made up of extensive medium- to high-grade metamorphic supracrustal rocks and subordinate granitoid gneisses, having been named as Milan and Dunhuang Complexes (Lu et al., 2008; Liu

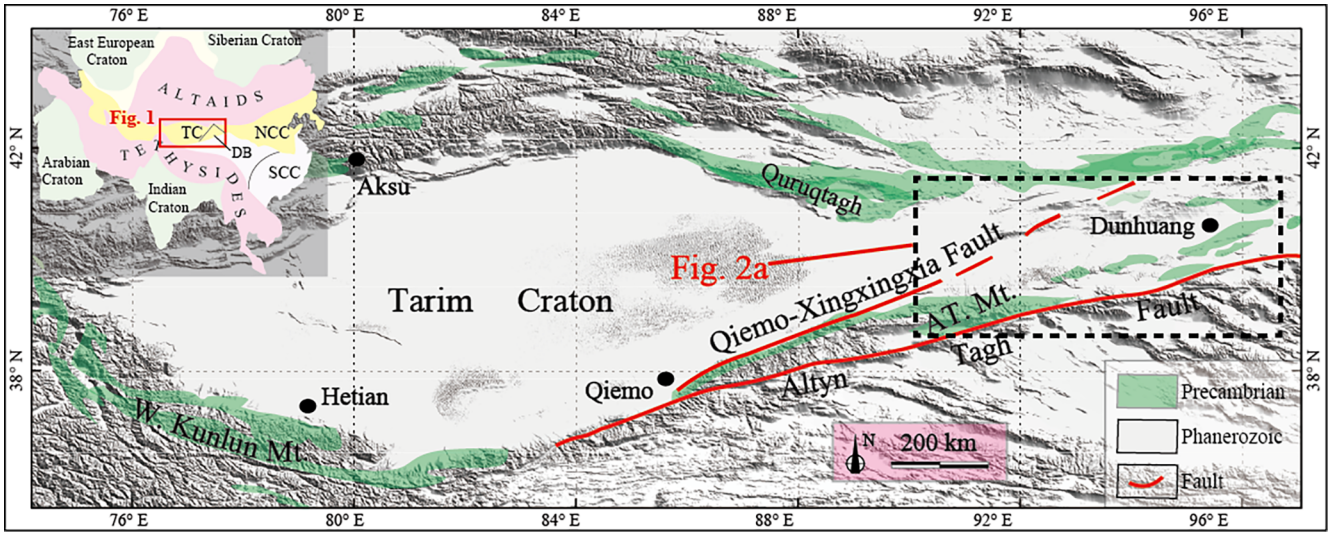


Fig. 1. Sketched tectonic and topographic map of the Tarim Craton and adjacent areas showing the distribution of the Precambrian basement outcrops (modified after Lu et al., 2008; Xu et al., 2011). Inset Figure shows a simplified tectonic map of the Dunhuang Block (modified after Xiao et al., 2010). TC-Tarim Craton; NCC-North China Craton; SCC-South China Craton; DB-Dunhuang Block.

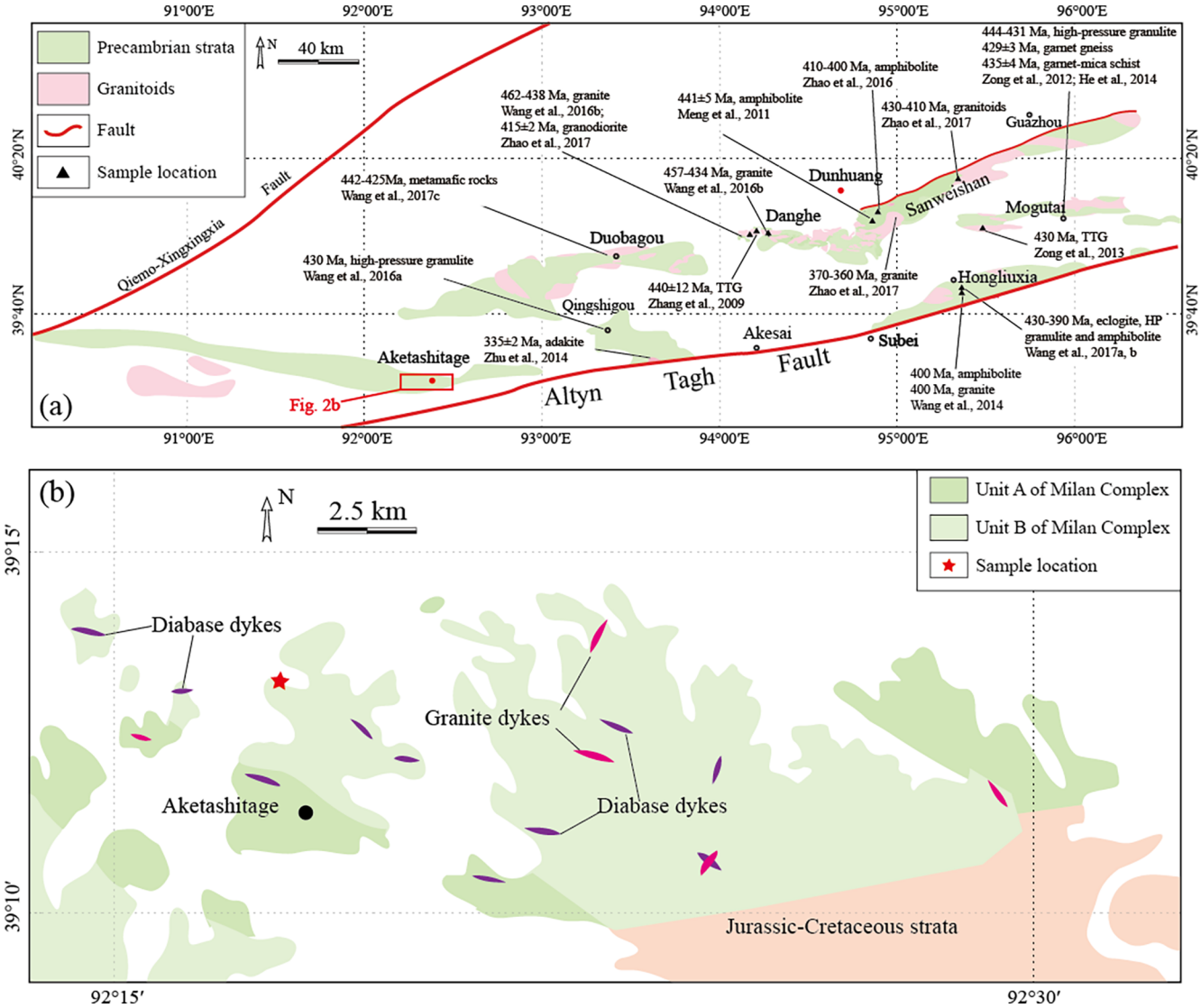


Fig. 2. (a) Simplified map of the Dunhuang Block showing locations of the Paleozoic magmatic and metamorphic rocks (modified after Wang et al., 2017e); (b) Simplified geologic map of the Aketashitage area, southwest Dunhuang Block (modified after the geological map of Eboliang 1:200000).

et al., 2009). The Dunhuang Complex is primarily composed of a large range of tonalite-trondhjemite-granodiorite (TTG) gneisses and supracrustal rocks, with the latter being defined as the Dunhuang Group and thought to be Archean-Paleoproterozoic in age (BGMRG, 1989; Mei et al., 1997; Yu et al., 1998; Lu, 2002b; Lu et al., 2006a,b). The dominant rock types of the Dunhuang Group are metasedimentary rocks, amphibolites, and mafic granulites. Findings of Paleoproterozoic amphibolite- to granulite-facies meta-mafic rocks in the Hongliuxia area, lead to argue that the Dunhuang Block was possibly associated with the assembly of the Columbia supercontinent (Zhang et al., 2012, 2013a; Wang et al., 2013; Zhao et al., 2013). Zircon U-Pb dating results of the TTG gneisses revealed that they were crystallized at 2.7–2.5 Ga and were modified by a Paleoproterozoic (2.0–1.8 Ga) high-grade metamorphic event (Zhang et al., 2013a; Zong et al., 2013). The Milan Complex is mainly distributed along the NE Altyn Tagh area, dominated by medium- to high-grade metamorphic rocks, including amphibolites, mafic granulites, felsic gneisses and marbles, as well as TTG-like gneisses. Previous studies reveal that the TTG-like gneisses of the Milan Complex have crystallization ages of 2.8–2.5 Ga and metamorphic ages of 1.9–2.0 Ga, and were intruded by 1.78–1.87 Ga post-tectonic granitic and mafic dykes (Lu and Yuan, 2003; Xin et al., 2011, 2012, 2013; Long et al., 2014). However, Ge et al. (2018) report a suit of newly discovered Eoarchean high-pressure TTGs with an age of ~ 3.7 Ga in the same area. The supracrustal rocks of the Milan Complex exhibit complicated features of deformation and metamorphism (Che and Sun, 1996; Lu et al., 2008). The deposition ages of their protoliths have not been well constrained, but they were intruded by 2.14–1.93 Ga pre- to syn-tectonic granitoids and carbonatites (Lu et al., 2008; Xin et al., 2011, 2013).

In this study, representative samples were collected from a single outcrop in the Aketashitage area, Dunhuang Block, southeastern Tarim Craton. Sample locations are presented in Fig. 2b. The study area is dominated by Archean orthogneisses with variable degrees of partial melting, including TTG rocks and monzogranitic gneisses, with tonalitic melanosomes and granitic leucosomes (Lu, 2002a; Long et al., 2014). The remaining rocks exposed in the study area mainly consist of paragneisses, amphibolites, granulites, quartzites and marbles. Most of these supracrustal rocks underwent intense deformation and commonly occur as layers or boudins within the Archean orthogneisses (Che and Sun, 1996; Lu, 2002b; Lu and Yuan, 2003). Both the supracrustal rocks and Archean orthogneisses were intruded by Paleoproterozoic granitic veins and younger mafic dykes (Fig. 3a). Samples selected for analyses were relatively fresh and contain no veins. In the field, it is typical that the analyzed mafic granulites occur as boudins or lenses within Grt-Bi

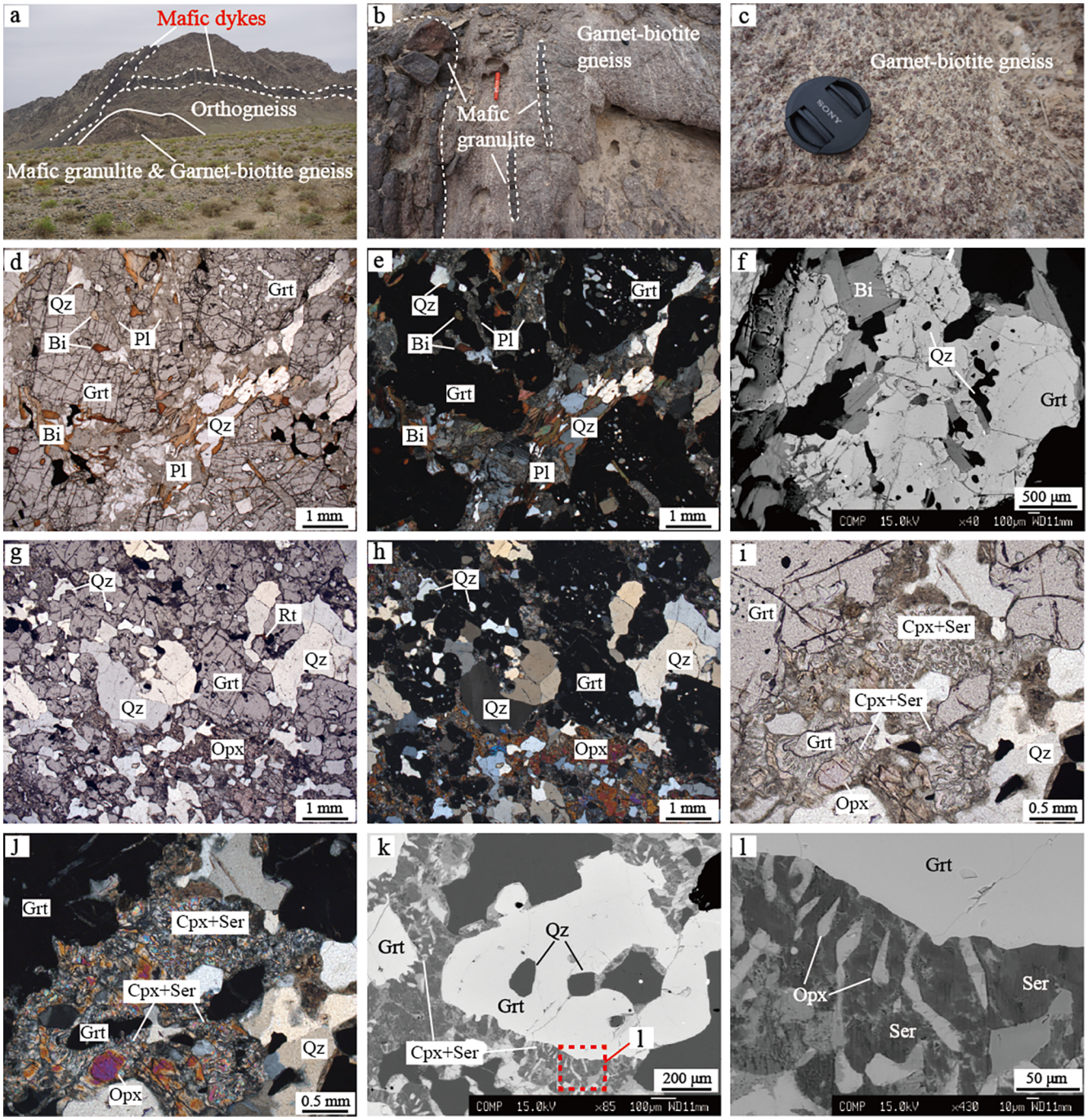


Fig. 3. Field photographs and photomicrographs of the studied granulite-facies metamorphic rocks in the Aketashitage area. (a) and (b) Field occurrence and relationship of garnet-biotite gneiss and mafic granulite; (c) Garnet-biotite gneiss is coarse-grained and weakly foliated; (d) and (e) Garnet-biotite gneiss have abundant porphyroblastic garnets and euhedral matrix minerals; (f) Typical textrue of the matrix biotite; (g) and (h) Large garnet porphyroblasts in the typical mafic granulite; (i) and (j) Garnet porphyroblasts are arounded by kelyphitic coronas in the mafic granulite; (k) and (l) Symplectitic plagioclase is extensively sericitized and almost exclusively replaced by sericite. Abbreviations: Grt-garnet; Bi-biotite; Pl-plagioclase; Qz-quartz; Opx-orthopyroxene; Cpx-clinopyroxene; Ser-sericite; Rt-rutile.

gneisses Fig. 3b. Occasionally, the contact is sharp but in most cases is transitional.

3. Analytical methods

3.1. Electron microprobe mineralogical analyses

Compositional analyses of representative minerals were conducted with a JEOL JXA-8100 electron microprobe (EMP) at the Institute of Geology and Geophysics, Chinese Academy of Sciences (IGGCAS) in Beijing, China. Operating conditions were 15 kV and 10nA with a 3 μm beam size. Counting times were 20 s for peaks and 10 s for each background. Natural and synthetic phases were used as standards. The data were processed with an online ZAF correction.

3.2. Zircon U-Pb dating and Hf isotopic analyses

Zircons were separated using heavy liquid and magnetic techniques

and then handpicked under a binocular microscope. The selected zircon grains were mounted in epoxy mounts which were then polished to section for analysis. The structures and inclusions of zircon grains were documented with transmitted and reflected light micrographs. To observe the internal structure and select a potential target site for U-Pb and Hf isotopic analyses, high-resolution cathodoluminescence (CL) imaging was conducted using a JXA8100 electron microprobe at IGGCAS.

Measurements of U, Th and Pb were conducted using the Cameca IMS-1280 SIMS at IGGCAS. The measurement procedures followed methods described by Li et al. (2009, 2010). U-Th-Pb ratios and absolute abundances were determined relative to the standard zircon Plesovice and 91500. The ellipsoidal spot is about 20 × 30 μm in size. The mass resolution used to measure Pb/Pb and Pb/U isotopic ratios was 5400 during the analyses. A long-term uncertainty of 1.5% (1 RSD) for $^{206}Pb/^{238}U$ measurements of the standard zircons was propagated to the unknowns (Li et al., 2009, 2010). Measured compositions were corrected for common Pb using non-radiogenic ^{204}Pb. Corrections were sufficiently small to be insensitive to the choice of a common Pb composition, and an average of present-day crustal compositions (Stacey and Kramers, 1975) was used for the common Pb assuming that the common Pb is largely surface contamination introduced during sample preparation. Uncertainties of individual analyses in the tables are reported at a 1σ level; concordia U-Pb ages are quoted with a 95% confidence interval. Data reduction was carried out using the Isoplot/Ex 3.0 program (Ludwig, 2003).

In situ Hf isotopic analyses were conducted by MC-ICP-MS at the IGGCAS, using the same Geolas-193 laser ablation system. Lu-Hf isotopic compositions were analyzed near the same spots where U-Pb analyses were carried out. A beam diameter of 44 μm was used for all the samples. The repetition rate was 8 Hz and the laser energy was 15 mJ/cm^2. Detailed analytical procedure and isobaric interference correction are reported in Wu et al. (2006) and Xie et al. (2008). During the analyses, the $^{176}Hf/^{177}Hf$ and $^{176}Lu/^{177}Hf$ ratios of the standard zircon (91500) were 0.282294 ± 15 ($2\sigma_n$, n = 20) and 0.00031 (Yang et al., 2006).

3.3. Whole-rock geochemical analyses

Samples were grounded in an agate mill to 200 mesh. Major oxides were determined by wavelength-dispersive X-ray fluorescence (XRF) spectrometry on fused glass at IGGCAS. The analytical precision was estimated to be better than 1% for elements with concentrations higher than 0.5 wt%. Trace element concentrations were analyzed by inductively coupled plasma mass spectrometry (ICP-MS) II at IGGCAS. We used pure elemental standards for external calibration and granite as a reference material. The accuracy of the analyses was better than 2.5%.

3.4. In situ trace element analyses of garnets

Trace element analyses of garnets were conducted by LA-ICP-MS at the Wuhan Sample Solution Analytical Technology Co., Ltd., Wuhan, China. Detailed operating conditions for the laser ablation system and the ICP-MS instrument and data reduction are the same as those described by Zong et al. (2017). Laser sampling was performed using a GeolasPro laser ablation system that consists of a COMPexPro 102 ArF excimer laser (wavelength of 193 nm and maximum energy of 200 mJ) and a MicroLas optical system. An Agilent 7700e ICP-MS instrument was used to acquire ion-signal intensities. Helium was applied as a carrier gas. Argon was used as the make-up gas and mixed with the carrier gas via a T-connector before entering the ICP. A “wire” signal smoothing device is included in this laser ablation system (Hu et al., 2014). The spot size and frequency of the laser were set to 44 μm and 5 Hz, respectively. Trace element compositions of garnets were calibrated against various reference materials (BHVO-2G, BCR-2G and BIR-1G) without using an internal standard (Liu et al., 2008). Each analysis incorporated a background acquisition of approximately 20–30 s followed by 50 s of data acquisition from the sample. An Excel-based software ICPMSDataCal was used to perform off-line selection and integration of background and analyzed signals, time-drift correction and quantitative calibration for trace element analysis (Liu et al., 2008).

4. Petrography, microtextures and mineral compositions

Representative major element compositions of garnet, orthopyroxene, clinopyroxene, and mica are given in Supplementary Tables 1–3. The trace element compositions of analyzed garnets are presented in Supplementary Table 4. Analyzed garnet grains are referred from now on by their host rocks. Garnets 16AK22, 16AK26-A and -B, and 16AK27 are from the corresponding samples with the same name.

4.1. Garnet-biotite gneiss (samples 16AK22, 23, and 24)

The garnet-biotite gneiss is coarse-grained, porphyroblastic, and weakly foliated, containing abundant garnet porphyroblasts (35–40%) in a foliated matrix mainly composed of plagioclase, biotite, and quartz (Fig. 3c). Common accessary minerals are magnetite, and in lesser amounts, rutile. Large garnet porphyroblasts frequently contain various inclusions, with lath-like plagioclase, sugar-like quartz and flake-like biotite (Fig. 3d, e and f). Matrix-minerals are generally presented as large and euhedral grains compared with those as inclusions within garnets. Matrix biotite commonly occurs as clots of crystals fill in the interstitial spaces of garnet porphyroblasts and align with the regional foliation (Fig. 3f). Quartz in the matrix occurs mainly as lobate or rounded megacryst and is unevenly distribute (Fig. 3d and e). Compositional transects in garnet 16AK24 show $Alm_{69}Prp_{23}Grs_5Sps_1$ as the core composition, with a progressive outward decrease in almandine and spessartine to the rim, although there is a slight increase at the outmost rim (Fig. 4a). The increase in X_{Fe} from the inner rim to outmost rim is most likely related to retrograde exchange reactions between garnet and biotite. The minor increase in X_{sps} at the outmost rim is probably the result of the retrograde kick-up effect (Kohn and Spear, 2000). Pyrope and grossular contents are essentially unzoned from core to rim (Fig. 4b). Chondrite-normalized REE patterns have no obvious variation in REE concentrations between core and rim (Fig. 5a). Both the core and rim are characterized by remarkable negative Eu anomalies and flat HREE patterns. As shown by Fig. 6a, the zoning profiles of Y, Ti, Cr, V, and Co are continuous from core to rim, suggesting that an equilibrium was maintained during garnet growth (Hickmott and Shimizu, 1990).

4.2. Mafic granulite (samples 16AK25, 26, and 27)

The mafic granulites are coarse-grained and dark in color. They have mineral assemblages typical of mafic granulites, with abundant garnet, orthopyroxene, clinopyroxene and quartz, and some plagioclase as well as accessory ilmenite, zircon, monazite and rutile. Large garnet porphyroblasts are commonly euhedral in morphology and typically contain abundant inclusions of rounded quartz (Fig. 3g and h); whereas, fine-grained garnet crystals are hypidioblastic with varying degrees of resorption associated with coronal or symplectitic reaction texture microdomains (Fig. 3i and j). In some localized domains, the development of the kelyphitic coronas around garnet replaces most of the garnet crystal. The coronas are represented by the intergrowth of orthopyroxene and plagioclase, with the symplectitic plagioclase is extensively sericitized and almost exclusively replaced by sericite (Fig. 3k and l). Matrix quartz generally occurs as interstitial phases in aggregates, shows evidence for high temperature intracrystalline recrystallization, such as undulatory extinction and subgrains (Fig. 3h). Subhedral orthopyroxene with inclusions of quartz is commonly related to the metamorphic peak conditions.

Garnets from sample 16AK26 vary considerably in composition

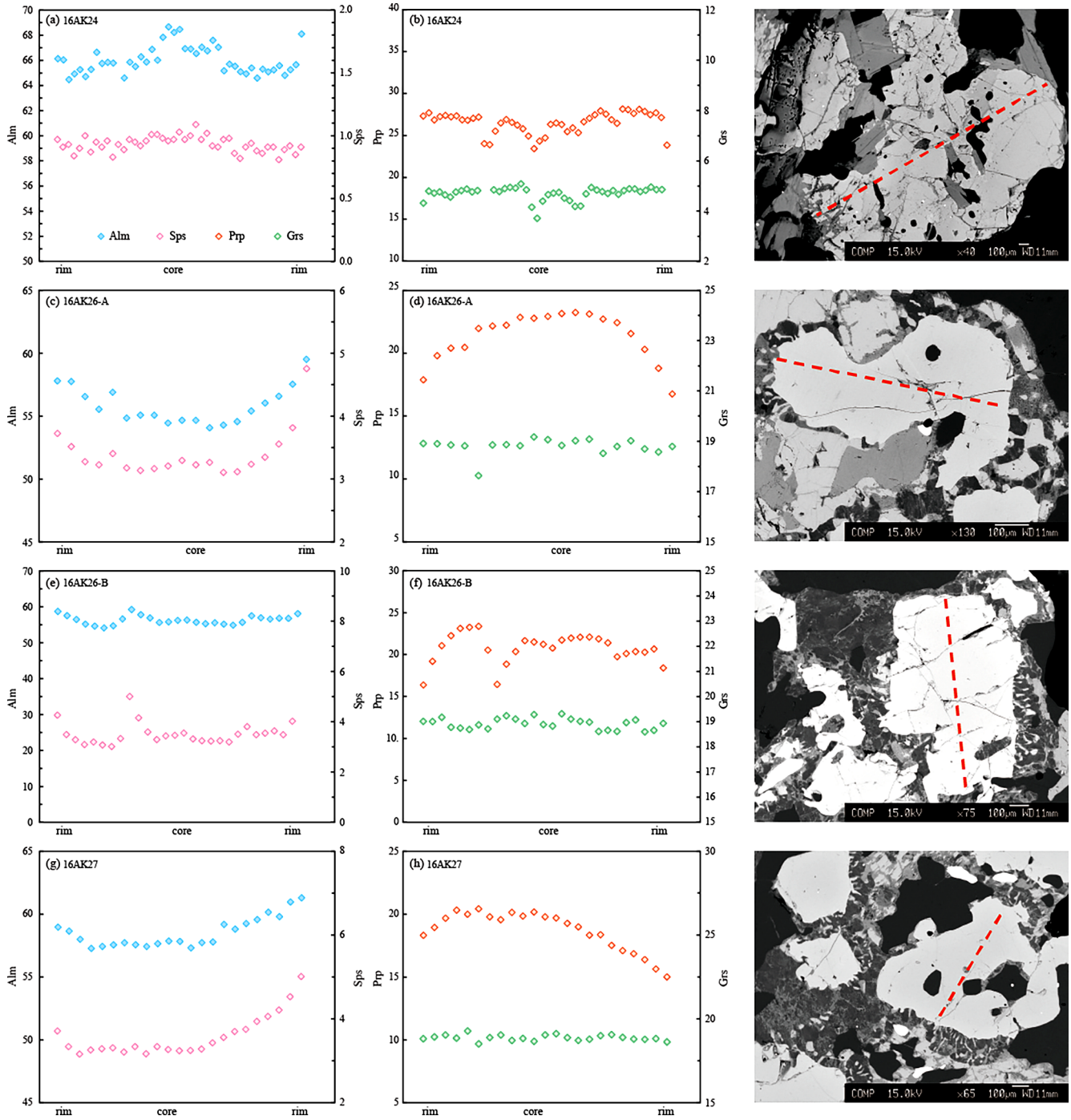


Fig. 4. The compositional profiles and BES images of the garnet porphyroblasts. Alm-almandine; Sps-spessartine; Prp-pyrope; Grs-grossular.

between different grains. Major element profile of garnet 16AK26-A shows a pronounced variation from core ($Alm_{55}Prp_{23}Grs_{19}Sps_3$) to rim ($Alm_{59}Prp_{17}Grs_{19}Sps_5$), with a marked increase in almandine and spessartine (Fig. 4c), and a sharp decrease in pyrope contents. Grossular contents are essentially unzoned (Fig. 4d). Whereas, the compositional transects of garnet 16AK26-B differ clearly from those of garnet 16AK26-A by exhibiting a wide plateau of homogeneous contents from core ($Alm_{56}Prp_{21}Grs_{19}Sps_4$) to rim ($Alm_{58}Prp_{18}Grs_{19}Sps_4$), suggesting limited modification during garnet growth (Fig. 4e and f). The slight variation of the outmost rim is related to retrograde reactions. However, the two aforementioned garnet grains have analogous chondrite-normalized REE patterns (Fig. 5b and c). Both of them display significant distinction between core and rim. Garnet cores are characterized by striking depletion in LREE, minor variation in HREE and strongly negative Eu anomalies. In contrast, the rims have more complicated REE patterns, which show variable concentrations in LREE and flat patterns in HREE. These two garnet grains have asymmetrical compositional zoning in terms of Y, Ti, Cr, V and Co, which display a homogeneous composition in the core, and decrease continuously toward the rims, with uniform contents in the outmost rims (Fig. 6b and c). The slight increases in Co, V and Cr in the outermost rim of garnet 16AK26-A may be caused by the involvement of magnetite and/or ilmenite in garnet growth. The decreases in Y and HREE for garnet 16AK26-B appear to be caused by clinozoisite growth coupled with variations in temperature and pressure (Hickmott and Spear, 1992). The low Y concentration in the garnet rim is might be controlled by

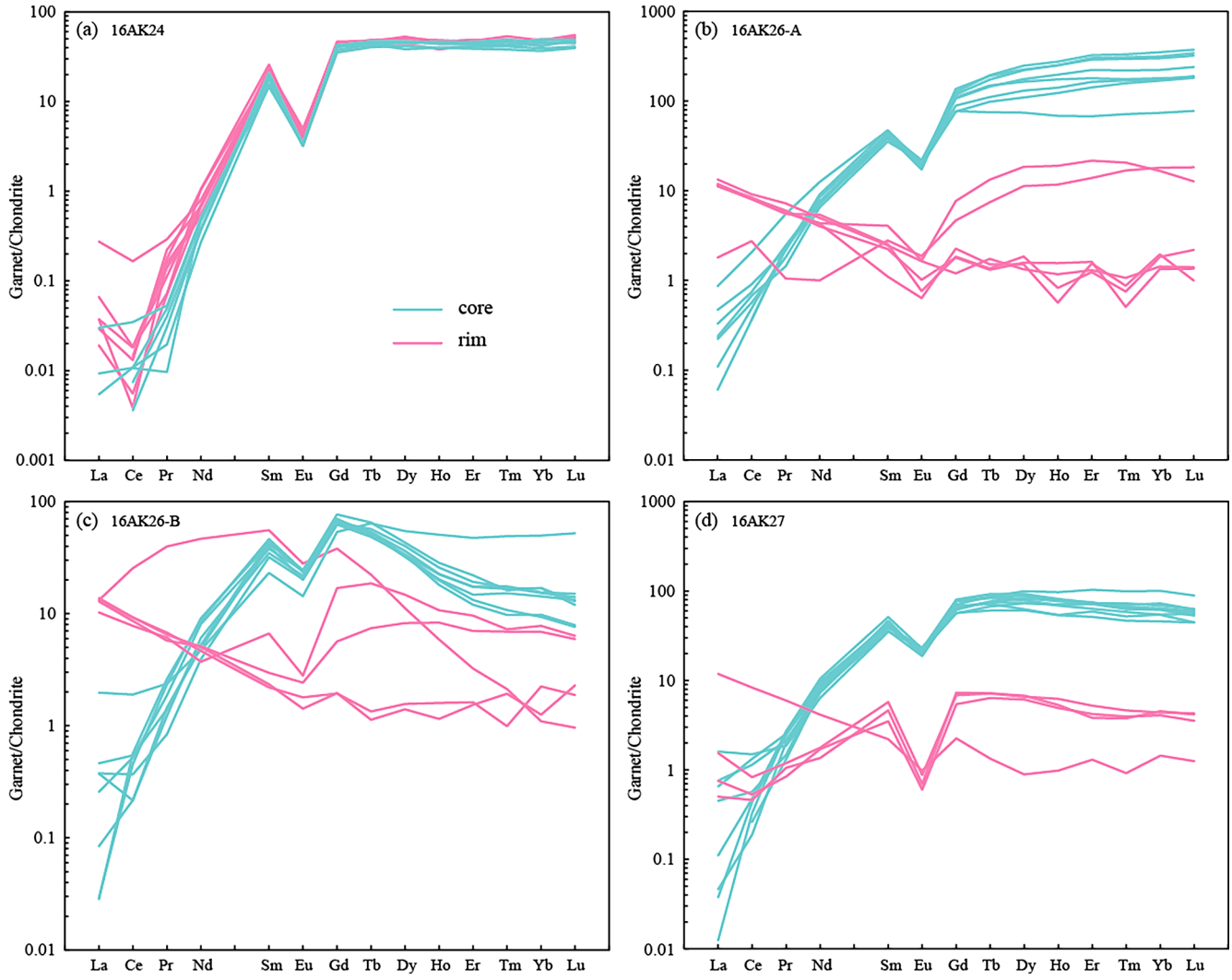


Fig. 5. Chondrite-normalized rare earth element diagrams of garnets in the granet-biotite gneiss and granulite. Chondrite-normalized values are from Sun and McDonough (1989).

growth of competing phases such as monazite. Mostly, the analyzed pyroxene in sample 16AK26 is orthopyroxene, and is chemically homogeneous (Supplementary Table 2). They have low jadeite (Na_2O = 0.05–0.18 wt%) and CaO (0.70–3.76 wt%) contents, although some variations exist in Al_2O_3 (17.4–18.1 wt%) and FeO (23.76–28.49 wt%) contents of different grains. Mica is sporadically developed in the matrix, and is homogeneous in composition.

Chemical composition profile across garnet 16AK27 (Fig. 4g and h) is characterized by an increase in almandine and spessartine, and a decrease in pyrope from core ($Alm_{58}Prp_{20}Grs_{19}Sps_3$) to rim ($Alm_{51}Prp_{15}Grs_{19}Sps_5$). Grossular displays slightly decreased zoning towards the outermost rim, interpreted as the consequence of decompression. The chondrite-normalized REE patterns (Fig. 5d) are characterized by progressive LREE- and HREE-depletion from core to rim. Garnet cores display steep chondrite-normalized REE patterns and strong negative Eu anomalies. Rims have flat REE patterns, with a slightly depletion in HREE and more pronounced negative Eu anomalies. With respect to the contents of Y, Ti, Cr, V and Co, they exhibit a homogeneous distribution in cores and a sharp decrease in rims (Fig. 6d). Pyroxene from sample 16AK27 is dominated by clinopyroxene in composition, and is chemically homogeneous (Supplementary Table 2). They have low contents in Na_2O (0.09–0.25 wt%) and Al_2O_3 (0.45–1.56 wt%), relatively high contents in CaO (21.82–22.74 wt%).

5. Metamorphic P-T conditions

Pressure-temperature (P-T) results are reported in Tables 1–3. The most serious drawback for a quantitative P-T determination of peak metamorphism is the lack of compositions relating to the complete equilibration between minerals. Thus, in the following discussion, only the retrograde P-T conditions are presented. The P-T estimates for the studied samples were obtained by combining relevant mineral chemistry information with conventional thermobarometers.

The texture and composition of the analyzed Grt-Bi gneiss reveal three-stage mineral assemblage: that is, the mineral inclusions enclosed in garnet porphyroblasts formed an earlier assemblage of Bi + Pl + Qz + Ilm, the garnet cores and matrix minerals form a peak mineral assemblage of Grt + Bi + Pl + Qz + Ilm ± Rt, and the retrograde assemblage is represented by the biotite those rimming the garnet or replacing garnet around the cracks. Unfortunately, in the absence of available barometers, the metamorphic pressure conditions are estimated roughly by the observed mineral assemblages. The rim compositions of the garnet porphyroblast and the rim compositions of the surrounding biotite were used to estimate the temperature conditions during retrograde metamorphism using a garnet-biotite Fe-Mg exchange thermometer. The average P-T conditions were determined to be 574 °C and 7.0 kbar, taken to represent the retrograde metamorphic P-T conditions of the Grt-Bi gneiss.

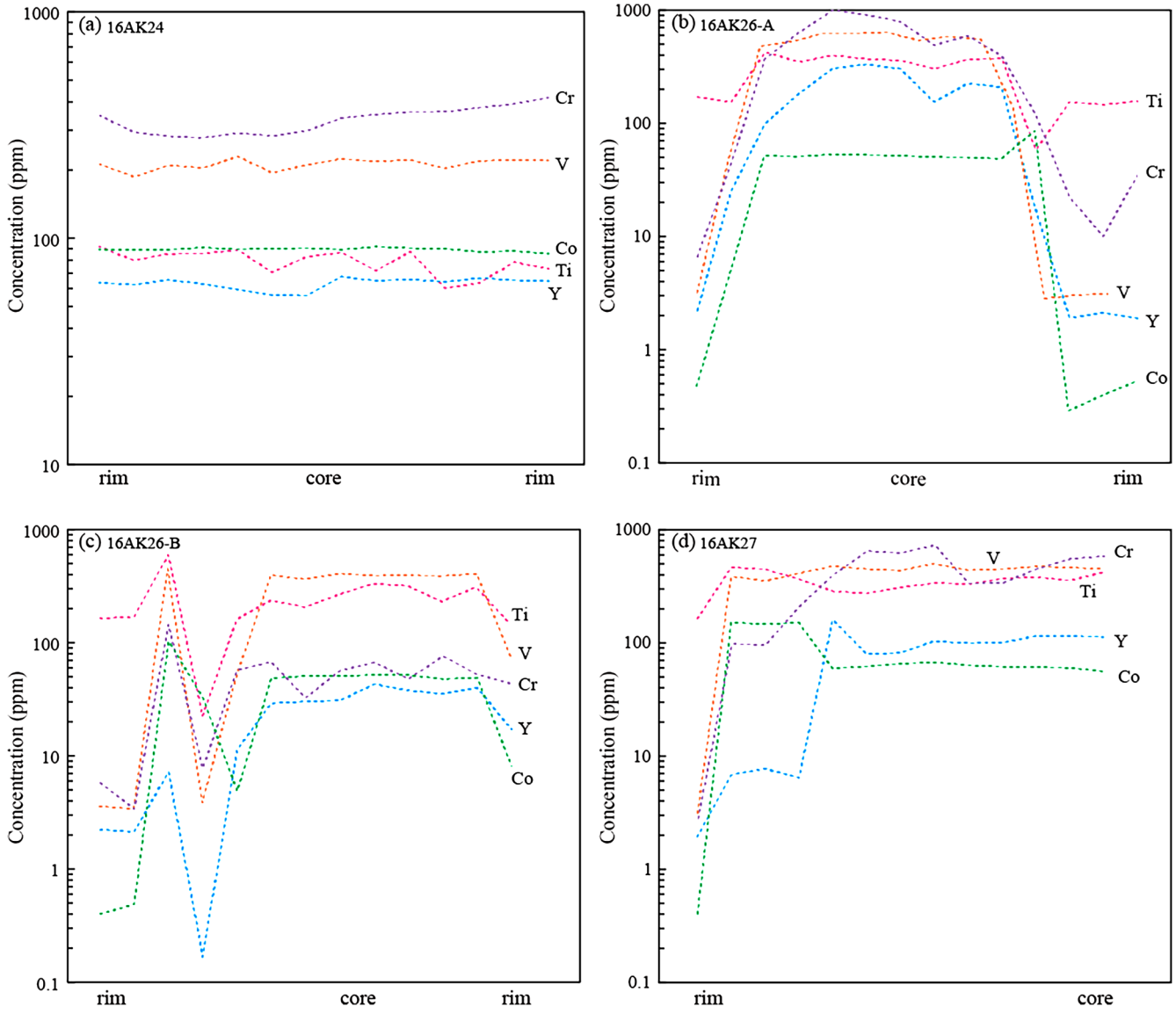


Fig. 6. Representative trace-element zoning in garnets from the granet-biotite gneiss and granulite.

Table 1
Retrograde P-T estimates for the analyzed samples.

Sample	Method (T&P)	T (°C)	P (kbar)
16AK24	Grt-Bi (Holdaway, 2000)	574	7.0
16AK26	Grt-Opx (Glebovitsky et al., 2004)	700	7.4
16AK27	Grt-Cpx (Berman et al., 1995)	715	7.0

For the mafic granulites, three episodes of metamorphic mineral assemblages are also preserved. The prograde assemblages are inclusion minerals (Pl + Qz + Ilm) enclosed in garnet porphyroblasts. The peak assemblages are formed by garnet porphyroblasts and matrix minerals (Grt + Cpx + Opx + Pl + Qz ± Ilm ± Rt), and the retrograde assemblages are represented by the symplectitic intergrowth of Cpx + Pl around the garnet. The garnet-orthopyroxene thermobarometry and the garnet-clinopyroxene thermometer are combined to estimate the P-T conditions during retrograde metamorphism. For sample 16AK26, compositions of garnet rim and orthopyroxene rim are used to calculate the retrograde P-T conditions, which gave averages of 700 °C and 7.4 kbar. For sample 16AK27, similar retrograde P-T conditions (T = 715 °C; P = 7.0 kbar) were given by garnet rim and associated clinopyroxene using the garnet-clinopyroxene thermometer. These estimated temperatures are considerably higher than that calculated for the Grt-Bi gneiss. However, both the Grt-Bi gneiss and mafic granulite have similar pressure estimations.

6. Zircon U-Pb ages and Hf isotopes

Cathodoluminescence (CL) images of representative zircon grains are shown in Fig. 7. Zircon U-Pb dating results and Hf isotopic compositions are reported in Tables 2 and 3. Analyses spots that are highly discordant with high errors are not shown and are excluded from calculations. Dated zircon crystals in both the Grt-Bi gneiss and mafic granulite samples were handpicked from the whole rock, that is, were found in the matrix, implying that these zircon grains were formed at peak metamorphism. They mostly preserve well-developed sector, patchy, fir-tree and planar zoning, which are common features in high-temperature metamorphic zircons produced through new zircon growth or by recrystallization (Vavra et al., 1999; Hoskin and Black, 2000; Hoskin and Schaltegger, 2003; Kelly and Harley, 2005; Harley et al., 2007).

Zircon grains from sample 16AK22 are rounded-ovoid or “soccer ball” in shape and variable in size, with crystal lengths of 50 to 100 μm. Most crystals are characterized by sector zoning, patchy and/or fir-tree

Table 2
U-Pb data for zircons from the analyzed garnet-biotite gneisses and mafic granulites.

Spot no.	Contnets		Ratios							Age(Ma)					
	Th	U	Th/U	$^{207}Pb/^{206}Pb$	1σ	$^{207}Pb/^{235}U$	1σ	$^{206}Pb/^{238}U$	1σ	$^{207}Pb/^{206}Pb$	1σ	$^{207}Pb/^{235}U$	1σ	$^{206}Pb/^{238}U$	1σ
16AK-22															
1	18	212	0.085	0.1174	0.6473	5.3685	1.6344	0.3318	1.5008	1916	12	1880	14	1847	24
2	30	214	0.140	0.1217	0.5834	6.3216	1.7101	0.3767	1.6075	1982	10	2021	15	2061	28
3	2	449	0.004	0.1177	0.7028	5.5198	1.6875	0.3403	1.5341	1921	13	1904	15	1888	25
4	24	342	0.071	0.1213	0.3082	5.9885	1.5871	0.3582	1.5569	1975	5	1974	14	1973	27
5	23	225	0.101	0.1174	0.7514	5.5580	1.7818	0.3433	1.6156	1917	13	1910	15	1903	27
6	10	260	0.038	0.1193	0.6838	5.4356	1.7415	0.3304	1.6016	1946	12	1890	15	1840	26
7	14	449	0.030	0.1209	0.7977	5.7892	1.7028	0.3473	1.5044	1970	14	1945	15	1922	25
8	13	443	0.029	0.1236	1.1132	5.9740	2.0765	0.3506	1.7528	2008	20	1972	18	1938	29
9	41	396	0.103	0.1194	0.6317	5.5579	1.7629	0.3375	1.6458	1948	11	1910	15	1875	27
10	7	227	0.032	0.1201	0.5197	5.9397	1.6001	0.3587	1.5133	1958	9	1967	14	1976	26
11	29	195	0.149	0.1181	0.9760	5.4675	1.8386	0.3359	1.5581	1927	17	1896	16	1867	25
12	17	279	0.060	0.1220	0.5666	5.9952	1.6052	0.3563	1.5019	1986	10	1975	14	1965	25
13	10	258	0.037	0.1188	0.5634	5.5615	1.6067	0.3396	1.5047	1938	10	1910	14	1885	25
14	5	489	0.010	0.1185	0.6040	5.7142	1.6170	0.3498	1.5000	1933	11	1934	14	1934	25
15	7	254	0.027	0.1266	0.4923	8.2052	4.7768	0.4700	4.7514	2052	9	2254	44	2483	99
16	29	244	0.119	0.1209	0.7127	5.9451	1.6670	0.3565	1.5069	1970	13	1968	15	1966	26
17	0	359	0.001	0.1175	0.4403	5.5686	1.5991	0.3438	1.5372	1918	8	1911	14	1905	25
18	35	258	0.137	0.1201	0.6427	5.3455	4.9163	0.3228	4.8741	1958	11	1876	43	1803	77
19	9	330	0.028	0.1203	0.7501	5.8250	1.6886	0.3512	1.5129	1960	13	1950	15	1940	25
20	52	369	0.141	0.1175	0.6392	5.5659	1.6499	0.3435	1.5211	1919	11	1911	14	1903	25
21	11	276	0.040	0.1207	0.8664	5.7699	1.8125	0.3468	1.5921	1966	15	1942	16	1919	26
22	10	287	0.034	0.1162	0.6567	5.5060	1.7363	0.3435	1.6073	1899	12	1902	15	1904	27
23	18	328	0.054	0.1192	0.8095	5.6560	1.7070	0.3442	1.5029	1944	14	1925	15	1907	25
24	11	473	0.024	0.1178	0.4628	5.6672	1.5991	0.3489	1.5307	1923	8	1926	14	1929	26
25	21	652	0.033	0.1189	0.3634	5.8917	1.5435	0.3595	1.5001	1939	6	1960	13	1980	26
16AK23															
1	20	579	0.035	0.1155	1.8648	4.1932	3.3738	0.2634	2.8116	1887	33	1673	28	1507	38
2	20	170	0.119	0.1189	0.6618	5.4884	1.6523	0.3349	1.5139	1939	12	1899	14	1862	25
3	11	371	0.030	0.1211	0.4023	5.6838	1.5651	0.3403	1.5125	1973	7	1929	14	1888	25
4	11	232	0.046	0.1221	0.6394	5.8899	1.6491	0.3498	1.5201	1987	11	1960	14	1934	25
5	11	214	0.053	0.1182	0.5352	5.4312	1.6025	0.3333	1.5105	1929	10	1890	14	1855	24
6	11	305	0.037	0.1248	0.9468	5.9694	1.7801	0.3470	1.5074	2026	17	1971	16	1920	25
7	18	314	0.056	0.1185	0.4536	5.6119	1.5683	0.3434	1.5013	1934	8	1918	14	1903	25
8	10	269	0.036	0.1192	0.8898	5.2119	1.7512	0.3171	1.5083	1945	16	1855	15	1775	23
9	31	427	0.072	0.1201	0.3466	5.7794	1.5448	0.3490	1.5054	1958	6	1943	13	1930	25
10	14	416	0.033	0.1232	1.0234	5.8990	1.8305	0.3474	1.5177	2002	18	1961	16	1922	25
11	13	386	0.033	0.1231	0.4976	5.9404	1.6196	0.3499	1.5413	2002	9	1967	14	1934	26
12	24	208	0.115	0.1214	0.8596	5.8590	1.7314	0.3499	1.5029	1978	15	1955	15	1934	25
13	10	284	0.036	0.1218	0.4632	5.7067	1.5923	0.3397	1.5235	1983	8	1932	14	1885	25
14	12	309	0.040	0.1175	0.5053	5.4735	1.6072	0.3378	1.5256	1919	9	1896	14	1876	25
15	16	590	0.028	0.1220	0.4482	5.5298	1.5933	0.3286	1.5290	1986	8	1905	14	1832	24
16	23	178	0.128	0.1176	0.8271	5.5132	1.7147	0.3399	1.5021	1921	15	1903	15	1886	25
17	11	403	0.026	0.1191	0.5001	5.6773	1.5893	0.3457	1.5086	1943	9	1928	14	1914	25
18	14	259	0.054	0.1169	3.5529	5.1560	3.8569	0.3199	1.5009	1909	62	1845	33	1789	23
19	8	342	0.023	0.1178	0.4808	5.4963	1.5779	0.3384	1.5028	1923	9	1900	14	1879	25
20	18	317	0.056	0.1166	0.4457	5.2639	1.6664	0.3275	1.6057	1904	8	1863	14	1826	26
21	11	292	0.037	0.1229	0.9800	6.1131	1.8065	0.3607	1.5175	1999	17	1992	16	1986	26
22	32	325	0.098	0.1201	0.4064	5.8100	1.5631	0.3509	1.5093	1957	7	1948	14	1939	25
23	11	278	0.040	0.1181	0.7365	5.6201	1.9694	0.3452	1.8265	1927	13	1919	17	1912	30
24	29	224	0.130	0.1168	0.5590	5.3799	1.6093	0.3342	1.5091	1907	10	1882	14	1859	24
25	14	306	0.045	0.1190	0.4579	5.7057	1.5702	0.3477	1.5019	1941	8	1932	14	1924	25
16AK24															
1	10	190	0.055	0.1217	0.4213	5.7557	1.5612	0.3431	1.5032	1981	7	1940	14	1902	25
2	12	195	0.061	0.1179	0.4095	5.6887	1.5638	0.3500	1.5092	1925	7	1930	14	1934	25
3	9	244	0.038	0.1173	0.4170	5.5238	1.5841	0.3416	1.5282	1915	7	1904	14	1894	25
4	238	648	0.367	0.1268	0.5632	5.6740	1.6040	0.3245	1.5018	2054	10	1927	14	1812	24
5	13	389	0.033	0.1206	0.4156	5.7281	1.5699	0.3446	1.5139	1964	7	1936	14	1909	25
6	11	324	0.034	0.1179	0.3770	5.6280	1.5795	0.3463	1.5339	1924	7	1920	14	1917	25
7	26	367	0.071	0.1213	0.4208	6.0117	1.5754	0.3594	1.5182	1976	7	1978	14	1979	26
8	21	336	0.063	0.1226	0.4557	5.9329	1.5691	0.3509	1.5015	1995	8	1966	14	1939	25
9	10	443	0.023	0.1202	0.4588	5.3959	1.5918	0.3256	1.5242	1959	8	1884	14	1817	24
10	284	377	0.753	0.1741	0.5589	11.1605	1.6069	0.4650	1.5066	2597	9	2537	15	2462	31
11	50	341	0.146	0.1194	0.3243	5.6397	1.5413	0.3426	1.5068	1947	6	1922	13	1899	25
12	100	596	0.168	0.1208	0.3279	5.8127	1.5389	0.3490	1.5035	1968	6	1948	13	1930	25
13	53	322	0.163	0.1213	0.4310	5.9051	1.5633	0.3531	1.5027	1975	8	1962	14	1950	25
14	12	320	0.039	0.1205	0.3179	5.9092	1.5448	0.3557	1.5117	1963	6	1963	14	1962	26
15	62	422	0.146	0.1210	0.4151	5.8370	1.5615	0.3498	1.5053	1971	7	1952	14	1934	25
16	56	339	0.164	0.1195	0.4172	5.8042	1.5846	0.3522	1.5287	1949	7	1947	14	1945	26
17	24	431	0.055	0.1225	0.5889	5.7993	1.6260	0.3433	1.5156	1993	10	1946	14	1903	25
18	15	431	0.034	0.1268	0.4110	6.3331	1.5611	0.3622	1.5060	2054	7	2023	14	1992	26

(*continued on next page*)

Table 2 (*continued*)

Spot no.	Contnets		Ratios							Age(Ma)					
	Th	U	Th/U	$^{207}Pb/^{206}Pb$	1σ	$^{207}Pb/^{235}U$	1σ	$^{206}Pb/^{238}U$	1σ	$^{207}Pb/^{206}Pb$	1σ	$^{207}Pb/^{235}U$	1σ	$^{206}Pb/^{238}U$	1σ
19	15	464	0.033	0.1252	0.3681	6.2520	1.5511	0.3622	1.5068	2031	7	2012	14	1993	26
20	19	431	0.044	0.1221	0.4408	5.9148	1.5667	0.3513	1.5034	1987	8	1963	14	1941	25
21	14	434	0.033	0.1219	0.3482	5.9627	1.5509	0.3549	1.5113	1984	6	1970	14	1958	26
22	11	176	0.060	0.1210	0.4686	5.8663	1.5854	0.3517	1.5145	1970	8	1956	14	1943	25
23	25	240	0.105	0.1215	0.5583	6.0697	1.6389	0.3622	1.5409	1979	10	1986	14	1993	26
24	51	367	0.139	0.1209	0.3516	5.9643	1.5463	0.3578	1.5058	1970	6	1971	14	1972	26
25	6	292	0.022	0.1205	0.4734	5.9941	1.5916	0.3609	1.5195	1963	8	1975	14	1986	26
1	291	2971	0.098	0.0916	0.3301	2.0276	1.5610	0.1606	1.5257	1459	6	1125	11	960	14
2	366	3281	0.111	0.1089	0.4218	3.0877	1.6245	0.2056	1.5688	1781	8	1430	13	1205	17
3	220	2241	0.098	0.1111	0.3451	3.7022	1.5516	0.2416	1.5127	1818	6	1572	12	1395	19
4	394	2064	0.191	0.0984	0.4788	2.5198	1.5814	0.1857	1.5072	1594	9	1278	12	1098	15
5	250	2072	0.121	0.1023	0.4176	2.7060	1.5648	0.1918	1.5080	1667	8	1330	12	1131	16
6	243	1856	0.131	0.1101	0.4769	3.5272	1.5740	0.2323	1.5000	1801	9	1533	13	1347	18
7	262	2515	0.104	0.0965	1.2646	2.5637	1.9627	0.1926	1.5010	1558	24	1290	14	1136	16
8	231	1981	0.117	0.1026	1.0615	2.9740	1.8480	0.2103	1.5127	1671	19	1401	14	1230	17
9	293	2035	0.144	0.1014	1.0916	2.8027	1.8899	0.2005	1.5427	1650	20	1356	14	1178	17
10	399	2285	0.175	0.1099	0.6347	3.2125	1.6373	0.2119	1.5093	1798	12	1460	13	1239	17
11	732	4095	0.179	0.1018	0.4286	2.9127	1.6113	0.2076	1.5533	1656	8	1385	12	1216	17
12	265	1993	0.133	0.1058	0.8511	3.2062	1.7283	0.2197	1.5042	1729	16	1459	13	1280	17
13	226	1490	0.151	0.1102	0.9325	3.6599	1.7936	0.2408	1.5321	1803	17	1563	14	1391	19
14	435	2513	0.173	0.0940	0.5094	1.7609	1.6615	0.1359	1.5815	1508	10	1031	11	821	12
15	40	2922	0.014	0.0991	0.4532	2.7462	1.6316	0.2009	1.5673	1608	8	1341	12	1180	17
16	192	1783	0.108	0.1063	0.6349	3.4757	1.9202	0.2371	1.8122	1737	12	1522	15	1371	22
17	267	3099	0.086	0.0961	0.7008	2.5409	1.6580	0.1917	1.5026	1550	13	1284	12	1131	16
18	243	2197	0.110	0.1011	1.8477	2.3471	2.3871	0.1684	1.5115	1645	34	1227	17	1003	14
19	293	3120	0.094	0.0829	2.3307	1.5936	2.7893	0.1394	1.5324	1267	45	968	18	841	12
20	468	4536	0.103	0.0954	0.4461	2.5486	1.5883	0.1937	1.5244	1537	8	1286	12	1141	16
21	226	2288	0.099	0.1127	0.3397	3.6689	1.5635	0.2360	1.5261	1844	6	1565	13	1366	19
22	81	872	0.093	0.1224	0.3615	5.0441	1.5709	0.2989	1.5287	1991	6	1827	13	1686	23
23	44	1021	0.043	0.1169	0.3787	4.2302	1.7259	0.2624	1.6839	1910	7	1680	14	1502	23
16AK26															
1	147	1388	0.106	0.1080	0.4392	3.3257	1.5949	0.2233	1.5332	1766	8	1487	13	1299	18
2	15	401	0.037	0.1189	1.2143	5.0396	1.9383	0.3073	1.5108	1940	22	1826	17	1728	23
3	252	1932	0.130	0.1014	0.3184	2.8564	1.5487	0.2044	1.5156	1649	6	1370	12	1199	17
4	293	2276	0.129	0.1001	0.6108	2.8365	1.6659	0.2055	1.5499	1626	11	1365	13	1205	17
5	230	2480	0.093	0.0939	0.9300	2.2782	1.7705	0.1760	1.5065	1506	17	1206	13	1045	15
6	99	2409	0.041	0.1050	0.8387	3.1836	2.3185	0.2200	2.1615	1714	15	1453	18	1282	25
7	269	2385	0.113	0.0997	1.2164	3.0927	1.9492	0.2250	1.5230	1618	22	1431	15	1308	18
8	265	2399	0.111	0.0894	0.3772	2.0723	1.5512	0.1681	1.5046	1413	7	1140	11	1002	14
9	134	1460	0.092	0.1076	0.3917	3.2377	1.5633	0.2182	1.5134	1759	7	1466	12	1273	18
10	212	1597	0.133	0.1080	0.3273	3.3341	1.5357	0.2239	1.5004	1766	6	1489	12	1303	18
11	299	2995	0.100	0.0987	0.7684	2.7976	1.6884	0.2056	1.5035	1600	14	1355	13	1205	17
12	243	1856	0.131	0.1018	1.3854	2.9996	3.5266	0.2136	3.2431	1658	25	1408	27	1248	37
13	264	2576	0.102	0.0889	0.3967	1.9780	1.5521	0.1613	1.5005	1402	8	1108	11	964	13
14	79	2276	0.035	0.1007	0.3930	2.8238	1.5866	0.2034	1.5371	1637	7	1362	12	1193	17
15	244	2499	0.098	0.1033	0.4412	2.9614	1.5642	0.2079	1.5007	1685	8	1398	12	1217	17
16	145	2382	0.061	0.0993	0.5308	2.8056	1.6042	0.2049	1.5139	1611	10	1357	12	1202	17
17	216	2038	0.106	0.1054	0.5188	3.0576	1.5961	0.2104	1.5094	1721	10	1422	12	1231	17
18	208	2361	0.088	0.1040	0.5475	3.1817	1.6351	0.2218	1.5407	1697	10	1453	13	1291	18
19	265	2474	0.107	0.1011	0.3393	2.9557	1.6648	0.2119	1.6298	1645	6	1396	13	1239	18
20	120	1499	0.080	0.1071	0.3570	3.3526	1.5453	0.2271	1.5035	1750	7	1493	12	1319	18
21	249	2478	0.101	0.1020	2.6944	2.9104	3.0842	0.2070	1.5010	1660	49	1385	24	1213	17
22	85	2650	0.032	0.1028	1.2338	3.2319	2.2082	0.2279	1.8314	1676	23	1465	17	1324	22
16AK27															
1	92	2461	0.037	0.1005	0.5831	3.0218	1.6112	0.2182	1.5020	1633	11	1413	12	1272	17
2	417	3775	0.110	0.0983	0.4905	2.7830	1.5965	0.2053	1.5193	1592	9	1351	12	1204	17
3	154	1478	0.104	0.1242	0.3474	6.4837	1.5966	0.3786	1.5583	2017	6	2044	14	2070	28
4	250	1864	0.134	0.1075	0.5133	3.4438	1.5961	0.2324	1.5113	1757	9	1514	13	1347	18
5	213	2227	0.095	0.1041	0.3503	2.9920	1.5411	0.2085	1.5008	1698	6	1406	12	1221	17
6	220	1696	0.130	0.1107	0.2462	3.2805	1.5222	0.2148	1.5021	1812	4	1476	12	1255	17
7	365	2270	0.161	0.1018	0.3817	2.8582	1.5478	0.2035	1.5000	1658	7	1371	12	1194	16
8	187	1345	0.139	0.1053	0.3544	3.0305	1.5573	0.2088	1.5164	1719	6	1415	12	1222	17
9	339	3265	0.104	0.0971	0.7261	2.8483	1.7678	0.2128	1.6118	1569	14	1368	13	1244	18
10	360	3683	0.098	0.1121	0.3093	3.2010	1.5415	0.2071	1.5101	1834	6	1457	12	1213	17
11	353	3305	0.107	0.1089	0.3811	3.1461	1.5512	0.2094	1.5037	1782	7	1444	12	1226	17
12	176	1497	0.117	0.1069	0.7237	3.2037	1.8323	0.2174	1.6834	1747	13	1458	14	1268	19
13	437	2910	0.150	0.0942	0.4136	2.2896	1.6140	0.1762	1.5601	1513	8	1209	11	1046	15
14	366	3708	0.099	0.0962	0.7426	2.8185	1.6742	0.2126	1.5005	1551	14	1360	13	1242	17
15	207	2150	0.096	0.1017	1.4205	2.9290	3.5778	0.2089	3.2837	1655	26	1389	27	1223	37
16	715	3194	0.224	0.0991	0.9319	3.0814	1.8113	0.2254	1.5532	1608	17	1428	14	1310	18
17	261	2766	0.094	0.1022	1.1608	2.9840	2.1501	0.2119	1.8098	1664	21	1404	16	1239	20
18	356	3552	0.100	0.0971	0.7833	2.4381	1.7137	0.1821	1.5241	1569	15	1254	12	1079	15

(*continued on next page*)

Table 2 (*continued*)

Spot no.	Contnets		Ratios							Age(Ma)					
	Th	U	Th/U	$^{207}Pb/^{206}Pb$	1σ	$^{207}Pb/^{235}U$	1σ	$^{206}Pb/^{238}U$	1σ	$^{207}Pb/^{206}Pb$	1σ	$^{207}Pb/^{235}U$	1σ	$^{206}Pb/^{238}U$	1σ
19	242	2014	0.120	0.1110	0.3830	3.3951	1.5687	0.2217	1.5213	1817	7	1503	12	1291	18
20	275	2810	0.098	0.0937	0.6109	2.0882	1.7936	0.1617	1.6864	1501	12	1145	12	966	15

zoning, while a few grains are unzoned with homogeneous internal structure (Fig. 7a). A total of 25 analyses recorded Th/U ratios ranging from 0.01 to 0.15 (mostly < 0.1) by SIMS, suggesting a metamorphic origin (Rubatto, 2002). Twenty-five analysis results fall on a discordant line with an upper intercept age of 1962 ± 18 Ma (MSWD = 1.13), which is similar, within analytical error, to the weighted mean $^{207}Pb/^{206}Pb$ age of 1952 ± 78 Ma (MSWD = 0.03) (Fig. 8a). Given the diagnostic characteristics of metamorphic zircons, this upper intercept age is taken to represent the metamorphic age of the Grt-Bi gneiss. Twenty-four dated zircons were performed for Hf isotopic analyses later. The obtained results are characterized by variable initial Hf compositions ($^{176}Hf/^{177}Hf_{(i)}$ = 0.280755–0.281497) and negative ε_{Hf} (t) values (from −4.6 to −0.6), with T_{DM}^{C} model ages ranging from 2709 to 2889 Ma (Fig. 9).

Zircons from sample 16AK23 are predominantly rounded and equant crystals, small in size with sector or planar zoning (Fig. 7b), indicative of a metamorphic origin. Meanwhile, they mostly exhibit low Th/U ratios (< 0.1). Twenty-five zircon grains were analyzed by SIMS for U-Pb ages. The obtained ages are concordant to variably discordant (Fig. 8b), falling on a discordia with an upper intercept age of 1977 ± 24 Ma (MSWD = 2.6), which is, within analytical uncertainties, consistent with the weighted mean $^{207}Pb/^{206}Pb$ age of 1951 ± 75 Ma (MSWD = 0.03). This age more likely represents the metamorphic age of the Grt-Bi gneiss. Twenty-five dated spots were analyzed for Hf isotopic compositions. They show a narrow range in initial Hf compositions ($^{176}Hf/^{177}Hf_{(i)}$ = 0.281191–0.281494) and large range in ε_{Hf} (t) values (from −11.7 to −1.5), with T_{DM}^{C} model ages scatter from 2704 to 3368 Ma (Fig. 9).

Zircon grains contained in sample 16AK24 have length-to-width ratios near to 1:1 and are predominantly rounded crystals with patchy zoning (Fig. 7c), indicative of metamorphic zircons. A total of twenty-five analyses were performed on these zircons, with majority of the data plotting on, or near, the concordant line (Fig. 8c), defining an upper intercept age of 1984 ± 26 Ma (MSWD = 3.5). Within analytical error, this age is consistent with the weighted mean $^{207}Pb/^{206}Pb$ age of 1971 ± 57 Ma (MSWD = 0.05), interpreted as best representing the metamorphic age of the Grt-Bi gneiss. All the dated zircons were selected for Hf isotopic analyses. Except for one grain with a positive ε_{Hf} (t) value (+2.5), the other zircons have highly variable negative ε_{Hf} (t) values between −1.0 and −15.0 (Fig. 9). Accordingly, they have relatively variable initial Hf ratios ($^{176}Hf/^{177}Hf_{(i)}$ = 0.281137–0.281508) and corresponding to T_{DM}^{C} model ages of 2672–3526 Ma.

Most zircons from sample 16AK25 are subrounded and small in size, with patchy zoning or are unzoned (Fig. 7d). Twenty-three zircon grains were analyzed for U-Pb compositions. Th/U ratios of these zircons vary from 0.01 to 0.19, indicative of metamorphic origin. The analytical results define a normal discordant line with an upper intercept age of 2036 ± 79 Ma (MSWD = 11) (Fig. 8d), representing the metamorphic age of the mafic granulite. Twenty-three dated spots were analyzed for Hf compositions. They have initial Hf compositions changing between 0.281113 and 0.281606. Their corresponding ε_{Hf} (t) values and T_{DM}^{C} model ages range from −18.2 to −3.0 and 2772 to 3648 Ma (Fig. 9), respectively.

Zircon grains in sample 16AK26 have crystal lengths range from 60 to 100 μm, and aspect ratios from 1:1 to 2:1. Ovoid morphology dominates most zircon crystals, although some grains display rounded terminations (Fig. 7e). Most crystals are essentially unzoned or have blurred zoning, typically diagnostic of metamorphic zircons. They have relatively low Th/U ratios between 0.03 and 0.13. A total of twenty-two analyses were conducted by SIMS. All the age data define a discordant line with an upper intercept age of age of 2016 ± 27 Ma (MSWD = 2.9) (Fig. 8e), taken to record the metamorphic age of the granulite. The dated zircon grains have relatively uniform initial $^{176}Hf/^{177}Hf$ ratios of 0.281450–0.281543, corresponding to highly variable ε_{Hf} (t) values between −14.4 and −1.8 (Fig. 9), resulting in T_{DM}^{C} model ages spread between 2706 and 3086 Ma.

Zircon grains from sample 16AK27 are mostly rounded crystals, with highly variable sizes between 80 and 150 μm. Their internal growth structure is characterized by convolute or planar zoning (Fig. 7f), a zoning pattern typically resulting from high-grade metamorphism (Vavra et al., 1999). They have Th/U ratios range between 0.04 and 0.22, predominantly < 0.1, suggesting a metamorphic origin. A total of twenty analytical spots defined a discordant line with an upper intercept age of 2003 ± 93 Ma (MSWD = 13.0) (Fig. 8f), which is taken to represent the metamorphic age of the granulite. All the dated zircons were selected for Hf isotopic analyses. They yielded relatively variable initial Hf ratios ($^{176}Hf/^{177}Hf_{(i)}$) of 0.281471–0.281620 and negative ε_{Hf}(t) values between −3.0 and −12.7 (Fig. 9), except one zircon grain (ε_{Hf} (t) = +1.1). The zircons with negative ε_{Hf} (t) values have T_{DM}^{C} model ages of 2655–3056 Ma.

7. Whole-rock major and trace element geochemistry

The analytical results of major and trace elements for samples are listed in Table 4. The least altered samples were selected for chemical analyses, and the major and trace element compositions can be used to identify the original geochemical characteristics of these metamorphic rocks.

The Grt-Bi gneisses show low contents in SiO_2 (52.0–53.2 wt%) and CaO (1.94–1.97 wt%), relatively high contents in Al_2O_3 (17.4–18.1 wt %) and total $Fe_2O_3^T$ (18.9–19.0 wt%), and moderate concentrations of MgO (4.92–4.96 wt%) and Na_2O (1.40–1.48 wt%). As the total alkali silica (TAS) diagram shows (Fig. 10), they have a basaltic-andesite affinity. With respect to trace element concentrations, the Grt-Bi gneisses have total REE contents ranging from 66 to 76 ppm. They have low and nearly flat chondrite-normalized REE patterns (Fig. 11a), with slightly negative Eu anomalies (Eu/Eu^* = 0.82–0.85). On the spider plots normalized to primitive mantle (Fig. 11b), the samples are relatively uniform and show moderately negative Nb-Ta and slightly positive Zr-Hf anomalies, and pronounced positive spikes in U and Pb. Generally, the analyzed samples exhibit low Nb/Ta and Zr/Hf ratios.

Mafic granulites have similar SiO_2 (49.3–54.7 wt%) content with Grt-Bi gneisses, higher concentrations of MgO (5.03–6.33 wt%), and relatively low total $Fe_2O_3^T$ (16.7–18.6 wt%), Al_2O_3 (13.7–14.8 wt%) and Na_2O (0.21–0.25) contents. The granulite samples have higher contents of some transition metals and HREE compared with Grt-Bi gneisses, reflecting their higher garnet and rutile contents. In the chondrite-normalized REE patterns (Fig. 11a), the granulite samples exhibit almost identical LREE and HREE normalized values, and thus, display a relatively flat pattern with insignificant negative Eu anomalies (Eu/Eu^* = 0.69–0.93). They have similar patterns with Grt-Bi gneisses on the primitive mantle-normalized spider diagram (Fig. 11a), except the less marked positive spike in Pb.

All the analyzed samples are strongly peraluminous in composition,

Table 3
Lu-Hf isotopic data of zircons from the analyzed garnet-biotite gneisses and mafic granulites.

Spot. No	Age (Ma)	$^{176}Yb/^{177}Hf$	1σ	$^{176}Lu/^{177}Hf$	1σ	$^{176}Hf/^{177}Hf$	1σ	$^{176}Hf/^{177}Hfi$	$e_{Hf}(t)$	$T_{DM1}(Hf)$	$T_{DM2}(Hf)$	T_{DM}^{C}	$f_{Lu/Hf}$
16AK22													
1	1916	0.00079	0.00002	0.00003	0.00000	0.28144	0.00001	0.281438	−4.5	2473	2829	2859	−1.00
2	1982	0.00052	0.00001	0.00002	0.00000	0.28147	0.00001	0.281468	−1.9	2432	2721	2746	−1.00
3	1921	0.00039	0.00001	0.00001	0.00000	0.28149	0.00001	0.281484	−2.7	2411	2725	2751	−1.00
4	1975	0.00040	0.00000	0.00001	0.00000	0.28146	0.00001	0.281453	−2.6	2453	2759	2786	−1.00
5	1917	0.00197	0.00014	0.00009	0.00001	0.28147	0.00001	0.281461	−3.6	2443	2778	2807	−1.00
6	1946	0.00305	0.00017	0.00012	0.00001	0.28142	0.00001	0.281416	−4.6	2504	2858	2889	−1.00
7	1970	0.00213	0.00015	0.00009	0.00001	0.28144	0.00001	0.281430	−3.5	2484	2811	2840	−1.00
8	2008	0.00627	0.00037	0.00029	0.00002	0.28145	0.00001	0.281434	−2.5	2481	2778	2805	−0.99
9	1948	0.00126	0.00004	0.00005	0.00000	0.28143	0.00001	0.281424	−4.2	2492	2839	2869	−1.00
10	1958	0.00094	0.00002	0.00003	0.00000	0.28143	0.00001	0.281430	−3.8	2484	2820	2849	−1.00
11	1927	0.00105	0.00004	0.00004	0.00000	0.28144	0.00001	0.281435	−4.3	2476	2828	2857	−1.00
12	1986	0.00052	0.00002	0.00002	0.00000	0.28144	0.00001	0.281440	−2.8	2470	2779	2807	−1.00
13	1938	0.00250	0.00025	0.00011	0.00001	0.28145	0.00001	0.281448	−3.6	2460	2793	2821	−1.00
14	1933	0.00170	0.00022	0.00007	0.00001	0.28144	0.00001	0.281435	−4.2	2477	2824	2853	−1.00
15	2052	0.00071	0.00001	0.00002	0.00000	0.28146	0.00001	0.281460	−0.6	2443	2693	2717	−1.00
16	1970	0.00060	0.00001	0.00002	0.00000	0.28148	0.00001	0.281479	−1.8	2417	2704	2729	−1.00
17	1918	0.00077	0.00003	0.00003	0.00000	0.28148	0.00001	0.281475	−3.1	2423	2747	2774	−1.00
18	1958	0.00104	0.00015	0.00004	0.00001	0.28146	0.00001	0.281452	−3.0	2455	2772	2800	−1.00
19	1960	0.00168	0.00031	0.00007	0.00002	0.28146	0.00001	0.281453	−3.0	2454	2768	2796	−1.00
20	1919	0.00062	0.00001	0.00002	0.00000	0.28145	0.00001	0.281451	−4.0	2455	2798	2827	−1.00
21	1966	0.00207	0.00035	0.00009	0.00002	0.28143	0.00001	0.281424	−3.8	2492	2826	2856	−1.00
22	1899	0.00166	0.00016	0.00007	0.00001	0.28145	0.00001	0.281445	−4.6	2464	2825	2855	−1.00
23	1944	0.00070	0.00001	0.00002	0.00000	0.28146	0.00001	0.281453	−3.3	2452	2777	2805	−1.00
25	1939	0.00049	0.00001	0.00002	0.00000	0.28150	0.00001	0.281497	−1.9	2393	2684	2709	−1.00
16AK23													
1	1887	0.01291	0.00050	0.00066	0.00003	0.28141	0.00001	0.281389	−6.9	2549	2955	2989	−0.98
2	1939	0.00137	0.00020	0.00006	0.00001	0.28146	0.00001	0.281452	−3.5	2455	2784	2812	−1.00
3	1973	0.00116	0.00007	0.00004	0.00000	0.28145	0.00001	0.281446	−2.9	2462	2775	2802	−1.00
4	1987	0.00355	0.00045	0.00017	0.00002	0.28144	0.00001	0.281431	−3.1	2483	2797	2825	−0.99
5	1929	0.00084	0.00002	0.00003	0.00000	0.28146	0.00001	0.281461	−3.4	2442	2771	2799	−1.00
6	2026	0.00062	0.00002	0.00002	0.00000	0.28139	0.00001	0.281390	−3.7	2537	2865	2894	−1.00
7	1934	0.00123	0.00001	0.00004	0.00000	0.28142	0.00001	0.281416	−4.9	2503	2866	2897	−1.00
8	1945	0.00548	0.00023	0.00026	0.00001	0.28145	0.00001	0.281441	−3.7	2472	2804	2833	−0.99
9	1958	0.00216	0.00019	0.00008	0.00001	0.28143	0.00001	0.281429	−3.9	2486	2822	2851	−1.00
10	2002	0.00530	0.00035	0.00026	0.00002	0.28146	0.00001	0.281448	−2.2	2462	2751	2778	−0.99
11	2002	0.00126	0.00014	0.00005	0.00001	0.28144	0.00001	0.281438	−2.5	2473	2774	2801	−1.00
12	1978	0.00068	0.00006	0.00002	0.00000	0.28145	0.00001	0.281444	−2.8	2464	2775	2803	−1.00
13	1983	0.00438	0.00036	0.00021	0.00002	0.28120	0.00002	0.281191	−11.7	2805	3325	3368	−0.99
14	1919	0.00047	0.00003	0.00002	0.00000	0.28148	0.00001	0.281476	−3.1	2422	2745	2772	−1.00
15	1986	0.00096	0.00001	0.00003	0.00000	0.28143	0.00001	0.281430	−3.2	2484	2801	2830	−1.00
16	1921	0.00113	0.00014	0.00004	0.00001	0.28144	0.00001	0.281436	−4.4	2475	2829	2859	−1.00
17	1943	0.00180	0.00009	0.00007	0.00000	0.28145	0.00001	0.281446	−3.6	2462	2793	2821	−1.00
18	1909	0.00754	0.00045	0.00038	0.00002	0.28146	0.00001	0.281445	−4.4	2468	2818	2847	−0.99
19	1923	0.00066	0.00013	0.00003	0.00001	0.28147	0.00001	0.281469	−3.2	2431	2757	2784	−1.00
20	1904	0.00055	0.00001	0.00002	0.00000	0.28146	0.00001	0.281459	−4.0	2444	2790	2818	−1.00
21	1999	0.00069	0.00001	0.00003	0.00000	0.28146	0.00001	0.281461	−1.8	2441	2724	2750	−1.00
22	1957	0.00430	0.00076	0.00021	0.00004	0.28150	0.00001	0.281494	−1.5	2400	2679	2704	−0.99
23	1927	0.00214	0.00017	0.00009	0.00001	0.28147	0.00001	0.281469	−3.1	2432	2754	2782	−1.00
24	1907	0.01408	0.00067	0.00063	0.00003	0.28138	0.00001	0.281357	−7.6	2592	3013	3048	−0.98
25	1941	0.00077	0.00001	0.00003	0.00000	0.28146	0.00001	0.281458	−3.2	2446	2769	2796	−1.00
16AK24													
1	1981	0.00101	0.00002	0.00004	0.00000	0.28147	0.00001	0.281467	−2.0	2434	2724	2750	−1.00
2	1925	0.00906	0.00086	0.00038	0.00003	0.28115	0.00003	0.281137	−15.0	2881	3479	3526	−0.99
3	1915	0.00244	0.00012	0.00010	0.00001	0.28140	0.00001	0.281390	−6.2	2538	2935	2968	−1.00
4	2054	0.01434	0.00034	0.00063	0.00002	0.28124	0.00001	0.281211	−9.4	2786	3235	3276	−0.98
5	1964	0.00791	0.00082	0.00039	0.00004	0.28149	0.00001	0.281477	−2.0	2425	2712	2738	−0.99
6	1924	0.00098	0.00001	0.00003	0.00000	0.28147	0.00001	0.281463	−3.4	2439	2768	2796	−1.00
7	1976	0.00073	0.00003	0.00002	0.00000	0.28148	0.00001	0.281480	−1.6	2417	2699	2724	−1.00
8	1995	0.00975	0.00088	0.00049	0.00004	0.28148	0.00001	0.281462	−1.8	2446	2726	2752	−0.99
9	1959	0.01127	0.00094	0.00054	0.00005	0.28153	0.00001	0.281508	−1.0	2385	2648	2672	−0.98
10	2597	0.02161	0.00065	0.00095	0.00003	0.28124	0.00001	0.281195	2.5	2800	2922	2937	−0.97
11	1947	0.00082	0.00001	0.00003	0.00000	0.28148	0.00001	0.281475	−2.5	2423	2728	2755	−1.00
12	1968	0.00087	0.00002	0.00003	0.00000	0.28142	0.00001	0.281418	−4.0	2500	2840	2870	−1.00
13	1975	0.00070	0.00003	0.00002	0.00000	0.28141	0.00001	0.281407	−4.2	2514	2860	2890	−1.00
14	1963	0.00045	0.00001	0.00001	0.00000	0.28143	0.00001	0.281423	−3.9	2493	2832	2861	−1.00
15	1971	0.00058	0.00001	0.00002	0.00000	0.28142	0.00001	0.281416	−4.0	2501	2841	2870	−1.00
16	1949	0.00056	0.00002	0.00002	0.00000	0.28140	0.00001	0.281400	−5.1	2523	2890	2921	−1.00
17	1993	0.00085	0.00001	0.00003	0.00000	0.28146	0.00001	0.281453	−2.2	2453	2747	2773	−1.00
18	2054	0.00076	0.00001	0.00002	0.00000	0.28143	0.00001	0.281431	−1.6	2482	2756	2782	−1.00
19	2031	0.00051	0.00002	0.00002	0.00000	0.28143	0.00001	0.281430	−2.1	2484	2773	2799	−1.00

(*continued on next page*)

Table 3 (*continued*)

Spot. No	Age (Ma)	$^{176}Yb/^{177}Hf$	1σ	$^{176}Lu/^{177}Hf$	1σ	$^{176}Hf/^{177}Hf$	1σ	$^{176}Hf/^{177}Hfi$	$e_{Hf}(t)$	$T_{DM1}(Hf)$	$T_{DM2}(Hf)$	T_{DM}^{C}	$f_{Lu/Hf}$
20	1987	0.00114	0.00003	0.00004	0.00000	0.28144	0.00001	0.281435	−3.0	2477	2791	2819	−1.00
21	1984	0.00094	0.00001	0.00003	0.00000	0.28145	0.00001	0.281447	−2.6	2461	2766	2793	−1.00
22	1970	0.00439	0.00050	0.00020	0.00002	0.28142	0.00001	0.281414	−4.1	2506	2845	2875	−0.99
23	1979	0.00054	0.00005	0.00002	0.00000	0.28146	0.00001	0.281461	−2.2	2441	2738	2764	−1.00
24	1970	0.00065	0.00001	0.00002	0.00000	0.28145	0.00001	0.281447	−2.9	2461	2775	2803	−1.00
25	1963	0.00616	0.00047	0.00027	0.00002	0.28147	0.00001	0.281461	−2.6	2444	2747	2774	−0.99
16AK25													
1	1459	0.00044	0.00003	0.00002	0.00000	0.28144	0.00001	0.281436	−14.9	2475	3126	3161	−1.00
2	1781	0.00038	0.00001	0.00002	0.00000	0.28142	0.00001	0.281419	−8.2	2498	2956	2990	−1.00
3	1818	0.00546	0.00035	0.00023	0.00001	0.28112	0.00001	0.281113	−18.2	2910	3599	3648	−0.99
4	1594	0.00042	0.00001	0.00002	0.00000	0.28137	0.00001	0.281371	−14.2	2563	3182	3220	−1.00
5	1667	0.00056	0.00001	0.00002	0.00000	0.28144	0.00001	0.281441	−10.0	2469	2983	3017	−1.00
6	1801	0.00058	0.00001	0.00002	0.00000	0.28142	0.00001	0.281415	−7.9	2504	2954	2988	−1.00
7	1558	0.00209	0.00049	0.00009	0.00002	0.28145	0.00001	0.281442	−12.5	2469	3050	3085	−1.00
8	1671	0.00192	0.00017	0.00009	0.00001	0.28141	0.00001	0.281404	−11.2	2519	3060	3096	−1.00
9	1650	0.00052	0.00002	0.00002	0.00000	0.28141	0.00001	0.281409	−11.6	2511	3063	3099	−1.00
10	1798	0.00243	0.00029	0.00011	0.00001	0.28139	0.00001	0.281389	−8.9	2540	3011	3047	−1.00
11	1656	0.00244	0.00003	0.00010	0.00000	0.28148	0.00001	0.281475	−9.1	2424	2913	2946	−1.00
12	1729	0.00209	0.00009	0.00009	0.00000	0.28154	0.00001	0.281532	−5.4	2349	2744	2773	−1.00
13	1803	0.00032	0.00001	0.00001	0.00000	0.28149	0.00001	0.281485	−5.4	2410	2799	2829	−1.00
14	1508	0.00054	0.00001	0.00002	0.00000	0.28152	0.00001	0.281518	−10.9	2367	2916	2949	−1.00
15	1608	0.00025	0.00002	0.00001	0.00000	0.28152	0.00001	0.281518	−8.6	2366	2851	2883	−1.00
16	1737	0.01227	0.00066	0.00052	0.00003	0.28132	0.00001	0.281299	−13.5	2670	3247	3288	−0.98
17	1550	0.00306	0.00056	0.00014	0.00003	0.28142	0.00001	0.281411	−13.7	2511	3122	3158	−1.00
18	1645	0.00037	0.00001	0.00002	0.00000	0.28147	0.00001	0.281463	−9.8	2439	2948	2982	−1.00
19	1267	0.00072	0.00002	0.00003	0.00000	0.28161	0.00001	0.281606	−13.2	2248	2876	2905	−1.00
20	1537	0.00130	0.00015	0.00005	0.00001	0.28143	0.00001	0.281428	−13.4	2487	3094	3130	−1.00
21	1844	0.00028	0.00002	0.00001	0.00000	0.28140	0.00001	0.281402	−7.4	2520	2953	2987	−1.00
22	1991	0.00268	0.00022	0.00012	0.00001	0.28144	0.00001	0.281432	−3.0	2482	2793	2821	−1.00
23	1910	0.00142	0.00008	0.00006	0.00000	0.28148	0.00001	0.281478	−3.2	2419	2744	2772	−1.00
16AK26													
1	1766	0.00232	0.00019	0.00011	0.00001	0.28149	0.00001	0.281485	−6.2	2411	2822	2853	−1.00
2	1940	0.00062	0.00002	0.00003	0.00000	0.28150	0.00001	0.281498	−1.8	2392	2681	2706	−1.00
3	1649	0.00039	0.00004	0.00002	0.00000	0.28150	0.00001	0.281498	−8.4	2393	2870	2902	−1.00
4	1626	0.00150	0.00018	0.00006	0.00001	0.28151	0.00001	0.281508	−8.6	2380	2860	2892	−1.00
5	1506	0.00068	0.00006	0.00003	0.00000	0.28151	0.00001	0.281508	−11.3	2380	2939	2972	−1.00
6	1714	0.00007	0.00001	0.00000	0.00000	0.28153	0.00001	0.281525	−6.0	2356	2768	2798	−1.00
7	1618	0.00039	0.00001	0.00001	0.00000	0.28152	0.00001	0.281514	−8.6	2372	2854	2886	−1.00
8	1413	0.00041	0.00001	0.00002	0.00000	0.28152	0.00001	0.281522	−12.9	2361	2967	2999	−1.00
9	1759	0.00022	0.00001	0.00001	0.00000	0.28152	0.00001	0.281522	−5.1	2361	2746	2775	−1.00
10	1766	0.00033	0.00001	0.00001	0.00000	0.28152	0.00001	0.281522	−4.9	2360	2741	2770	−1.00
11	1600	0.00038	0.00002	0.00001	0.00000	0.28152	0.00001	0.281521	−8.7	2361	2849	2881	−1.00
12	1658	0.00036	0.00002	0.00001	0.00000	0.28152	0.00001	0.281522	−7.4	2360	2810	2841	−1.00
13	1402	0.00009	0.00000	0.00000	0.00000	0.28149	0.00001	0.281486	−14.4	2408	3053	3086	−1.00
14	1637	0.00034	0.00005	0.00002	0.00000	0.28155	0.00001	0.281543	−7.1	2332	2777	2807	−−1.00
15	1685	0.00034	0.00001	0.00001	0.00000	0.28151	0.00001	0.281507	−7.3	2381	2826	2857	−1.00
16	1611	0.00018	0.00000	0.00001	0.00000	0.28150	0.00001	0.281503	−9.1	2386	2882	2915	−1.00
17	1721	0.00045	0.00002	0.00002	0.00000	0.28152	0.00001	0.281514	−6.2	2372	2788	2818	−1.00
18	1697	0.00140	0.00029	0.00006	0.00001	0.28147	0.00001	0.281469	−8.3	2432	2901	2934	−1.00
19	1645	0.00043	0.00001	0.00002	0.00000	0.28149	0.00001	0.281483	−9.0	2412	2904	2936	−1.00
20	1750	0.00057	0.00007	0.00002	0.00000	0.28149	0.00001	0.281488	−6.5	2406	2826	2857	−1.00
21	1660	0.00552	0.00065	0.00026	0.00003	0.28146	0.00001	0.281450	−9.9	2462	2967	3001	−0.99
22	1676	0.00006	0.00000	0.00000	0.00000	0.28150	0.00001	0.281494	−7.9	2397	2859	2891	−1.00
16AK27													
1	1633	0.00091	0.00005	0.00003	0.00000	0.28149	0.00001	0.281490	−9.1	2403	2896	2929	−1.00
2	1592	0.00059	0.00003	0.00002	0.00000	0.28154	0.00001	0.281539	−8.2	2337	2814	2845	−1.00
3	2017	0.00052	0.00001	0.00002	0.00000	0.28153	0.00001	0.281529	1.1	2351	2564	2584	−1.00
4	1757	0.00039	0.00002	0.00002	0.00000	0.28151	0.00002	0.281512	−5.5	2374	2769	2799	−1.00
5	1698	0.00042	0.00002	0.00002	0.00000	0.28150	0.00001	0.281501	−7.2	2388	2830	2862	−1.00
6	1812	0.00064	0.00003	0.00003	0.00000	0.28152	0.00001	0.281516	−4.1	2368	2724	2752	−1.00
7	1658	0.00098	0.00001	0.00004	0.00000	0.28156	0.00001	0.281552	−6.3	2321	2744	2774	−1.00
8	1719	0.00036	0.00000	0.00001	0.00000	0.28150	0.00002	0.281499	−6.8	2391	2821	2852	−1.00
9	1569	0.00115	0.00008	0.00004	0.00000	0.28154	0.00002	0.281533	−9.0	2346	2842	2874	−1.00
10	1834	0.00061	0.00001	0.00002	0.00000	0.28154	0.00001	0.281533	−3.0	2346	2674	2700	−1.00
11	1782	0.00053	0.00001	0.00002	0.00000	0.28154	0.00001	0.281537	−4.0	2340	2698	2725	−1.00
12	1747	0.00049	0.00002	0.00002	0.00000	0.28155	0.00001	0.281546	−4.5	2328	2700	2728	−1.00
13	1513	0.00079	0.00001	0.00003	0.00000	0.28154	0.00001	0.281536	−10.2	2343	2874	2905	−1.00
14	1551	0.00121	0.00005	0.00004	0.00000	0.28153	0.00001	0.281532	−9.4	2348	2858	2889	−1.00
15	1655	0.00104	0.00011	0.00004	0.00000	0.28148	0.00001	0.281473	−9.2	2427	2920	2953	−1.00
16	1608	0.00441	0.00007	0.00016	0.00000	0.28163	0.00002	0.281620	−5.0	2232	2628	2655	−1.00
17	1664	0.00078	0.00002	0.00003	0.00000	0.28152	0.00001	0.281520	−7.3	2363	2811	2842	−1.00

(*continued on next page*)

Table 3 (*continued*)

Spot. No	Age (Ma)	$^{176}Yb/^{177}Hf$	1σ	$^{176}Lu/^{177}Hf$	1σ	$^{176}Hf/^{177}Hf$	1σ	$^{176}Hf/^{177}Hfi$	$e_{Hf}(t)$	$T_{DM1}(Hf)$	$T_{DM2}(Hf)$	T_{DM}^{C}	$f_{Lu/Hf}$
18	1569	0.00101	0.00003	0.00004	0.00000	0.28152	0.00001	0.281519	−9.5	2365	2874	2906	−1.00
19	1817	0.00043	0.00001	0.00002	0.00000	0.28148	0.00001	0.281474	−5.5	2424	2813	2843	−1.00
20	1501	0.00029	0.00000	0.00001	0.00000	0.28147	0.00001	0.281471	−12.7	2428	3022	3056	−1.00

Note: $\varepsilon_{Hf}(t) = (((^{176}Hf/^{177}Hf)_S - (^{176}Lu/^{177}Hf)_S \times (e^{\lambda t} - 1))/((^{176}Hf/^{177}Hf)_{CHUR,0} - (^{176}Lu/^{177}Hf)_{CHUR} \times (e^{\lambda t} - 1)) - 1) \times 10000$; $T_{DM1}(Hf) = 1/\lambda \times \ln(1 + ((^{176}Hf/^{177}Hf)_S - (^{176}Hf/^{177}Hf)_{DM})/((^{176}Lu/^{177}Hf)_S - (^{176}Lu/^{177}Hf)_{DM}))$; $T_{DM2}(Hf) = T_{DM1}(Hf) - (T_{DM1}(Hf) - t)((fcc - fs)/(fcc - f_{DM}))$; $T_{DM}^{c} = (1/k) - \ln[1 + (^{176}Hf/^{177}Hf_{DM} - ^{176}Hf/^{177}Hf_S)/(^{176}Lu/^{177}Hf_{DM} - ^{176}Lu/^{177}Hf_S)]$; $f_{Lu/Hf} = (^{176}Lu/^{177}Hf)_S/(^{176}Hf/^{177}Hf)_{CHUR} - 1$; where $f_{CC,}$ f_S and f_{DM} are the $f_{Lu/Hf}$ values of the continental crust, sample and the depleted mantle; t = crystallization age of zircon; subscript S = analyzed sample, CHUR = chondritic uniform reservoir, DM = depleted mantle.

with the Grt-Bi gneisses showing higher A/CNK values (2.33–2.34) than mafic granulites (A/CNK = 1.22–1.25). Both the Grt-Bi gneiss and mafic granulite have flat REE patterns with negative Eu anomalies, resembling the REE patterns of mid-crust level garnets. These garnets tend to lose their negative fractionation pattern compared with garnets of more epizonal levels, thus acquiring a flatter pattern (Bea, 1996; Villaseca et al., 1999). All analyzed samples are characterized by higher LREE and HREE contents in comparison with estimated lower continental crust of Rudnick and Gao (2003).

8. Discussion

8.1. Interpretation and significance of zircon data

Processes of zircon-forming, zircon-consuming and zircon-modifying are generally controlled by rock composition, pressure and fluid-melt-rock interaction (Harley et al., 2007).

SIMS zircon U-Pb dating results from six samples indicate the presence of a well-defined age group, which covers a long time interval up to 70 Myr (from ca. 2036 to 1962 Ma). Hoskin and Black (2000) pionted out that the large spread in ages is likely to represent incomplete resetting of U-Pb isotopic compositions due to varying degrees of partial recrystallization. Therefore, the youngest ages represent more complete recrystallization and probably provide the best approximation to the timing of the recrystallization-including events (Hoskin and Black, 2000). Alternative, this kind of noticeable scatter in ages is probably resulted from pre- and post-peak high-temperature reactions, deformation and/or fluid ingress (Harley et al., 2007). Zircon formed by complete recrystallization of protolith zircon displays no internal structures, except for possible weak sector zonation (Hoskin and Black, 2000). When the recrystallization of protolith zircon is incomplete, zircon crystals may display internal textural characteristics including areas where oscillatory zoning is preserved and unzoned areas where zoning has been destroyed (Hoskin and Black, 2000). In our study, it is noteworthy that some zircon crystals in sample 16AK22 are shaped in “soccer ball”, typical of growth from a melt (Harley et al., 2007). Thus, the age of 1962 ± 18 Ma given by sample 16AK22 provides a preferable constraint on the timing of melt crystallization. Dating results record a large age span from 2036 to 1962 Ma given by mafic granulite (sample 16AK25) and Grt-Bi gneiss (sample 16AK22), respectively. As already mentioned, the large spread in ages is likely to be resulted from varying degrees of partial recrystallization, and the youngest ages possibly provide the best approximation to the timing of melt recrystallization. Given the above, age data of the Grt-Bi gneiss and mafic granulite samples indicate a main stage of melt recrystallization at ca. 1962 Ma recorded by the Grt-Bi gneiss (sample 16AK22). Moreover, the long duration of high-grade metamorphic ages indicate that these rocks were metamorphosed in a tectonic setting that prevailed for long periods and where large amounts of magmas were added to the crust uninterruptedly. In summary, zircon U-Pb data of the Grt-Bi gneisses and mafic granulites reveal that the study area experienced Paleoproterozoic granulite-facies metamorphism, which appears to have been a long-lived process, being sustained for over 70 Myr.

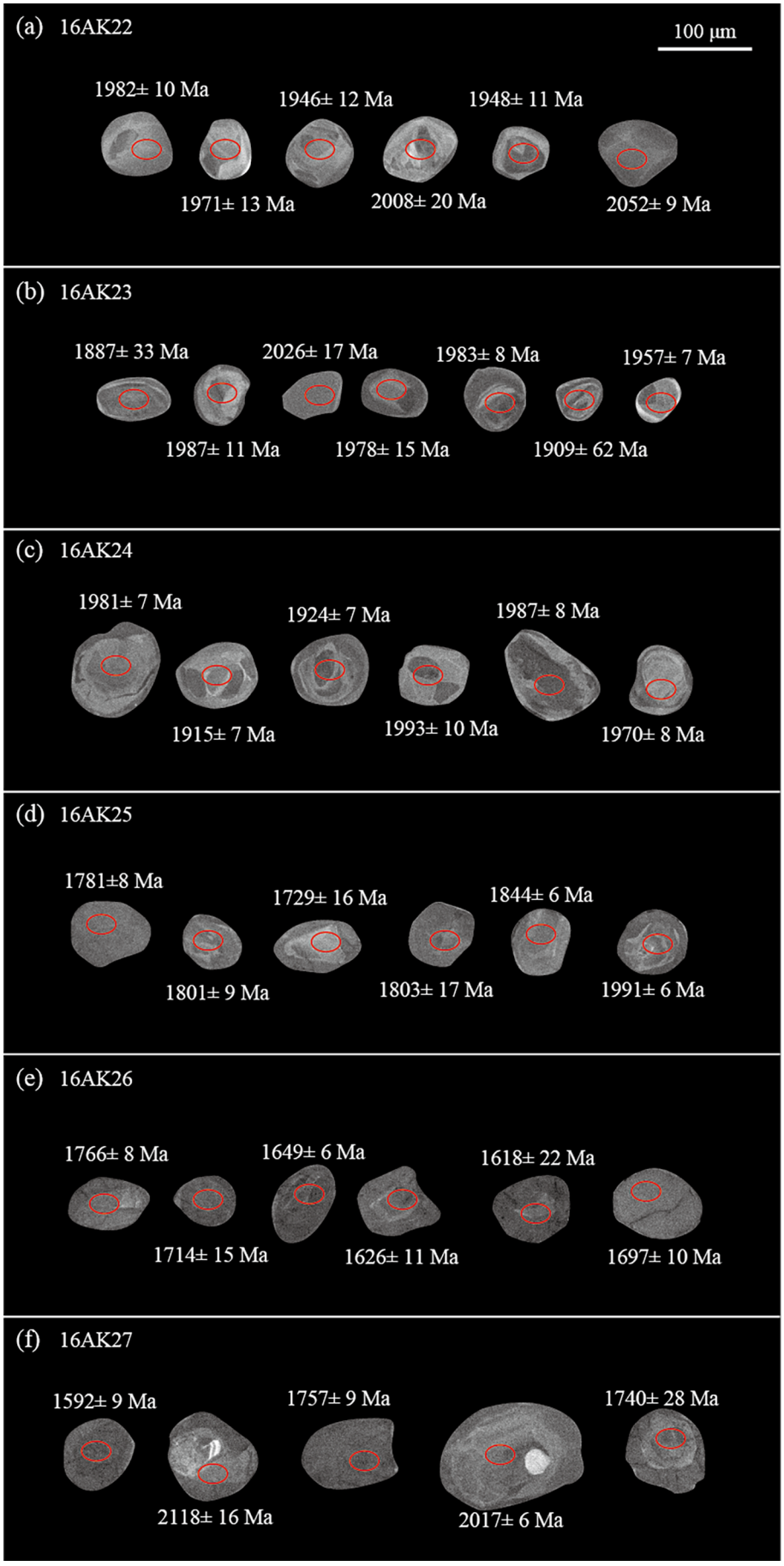
Analytical results of zircon Hf isotopes from both the Grt-Bi gneisses and mafic granulites reveal that they have variable but mostly negative ε_{Hf} (t) values (from −18.2 to −0.6), fairly uniform Hf isotopic compositions, and highly variable T_{DM}^{C} model ages ranging from 2628 to 3599 Ma. Notably, the large variation in Hf crustal model ages was mirrored exactly by the long time span of zircon ages. These distinctive negative ε_{Hf} (t) values, initial Hf isotopic compositions, and Hf crustal model ages are generally consistent with those from a Hf-in-zircon study for orthogneisses reported in the Lapeiquan area (Long et al., 2014). These data suggest a long-lived reworking of Archean crust in southern Tarim Craton during the Paleoproterozoic.

8.2. Granulite-facies metamorphism and recrystallization

The retrograde metamorphic reactions recorded by the Grt-Bi gneisses occur under P-T conditions of 574 °C and 7.0 kbar, and the calculated retrograde P-T conditions for the mafic granulites are roughly at 700 °C and 7.4 kbar, suggesting much higher metamorphic peak pressures and temperatures. Zircon grains from three Grt-Bi gneiss samples provide metamorphic ages covering a range of 1962–1984 Ma. The external morphology and internal structure, as well as Th/U ratios of zircons from Grt-Bi gneisses suggest that they have a metamorphic origin, and were probably produced by extensive melt recrystallization. The metamorphic-origin zircons from the mafic granulites give an age range of 2003–2036 Ma, which is consistent with the previously reported magmatism and metamorphism in the study area (Long et al., 2014; Wang et al., 2017c). Considering the dating uncertainty, it remains unclear whether the older age cluster records an earlier metamorphic event and the younger one records another, or both of them record different stages of the same event. Based on their field occurrences, mineral assemblages and compositions, as well as the typical diagnostic of zircon crystals, it is reasonable to be concluded that the age clusters given by the Grt-Bi gneisses and mafic granulites represent a long-lasting recrystallization-included granulite-facies metamorphism.

8.3. Regional implications

The late Paleoproterozoic magmatic and metamorphic activities with ages of 2.1–1.8 Ga are well-documented in the Tarim Craton (Lu et al., 2008; Ge et al., 2013a, 2013b, 2015; Wang et al., 2013, 2014, 2017c, 2017d; Long et al., 2014, 2015; Zhao et al., 2015b), and as they are in other continents, have been considered to be probably related to the assembly of the Columbia supercontinent (Condie, 2002; Rogers and Santosh, 2002; 2003; Zhao et al., 2002, 2004; Michael, 2007; Zhao and Cawood, 2012). Globally, the assembly of detached continental blocks generates collisional orogens along the colliding margins and is usually marked by high-grade regional metamorphism. For the Tarim Craton, the Paleoproterozoic high-grade metamorphism associated with the assembly of the Columbia supercontinent was mostly reported along its northern margin (Lu et al., 2006a,b; Long et al., 2011; Ge et al., 2013a; He et al., 2013; Xu et al., 2013). Whereas, the well-developed high-grade metamorphism in the southeastern margin of the



(caption on next page)

Fig. 7. Representative Cathodoluminescence (CL) images and corresponding ages for zircons from the studied samples. The red circles show the locations of U-Pb dating. (For interpretation of the references to color in this figure legend, the reader is referred to the web version of this article.)

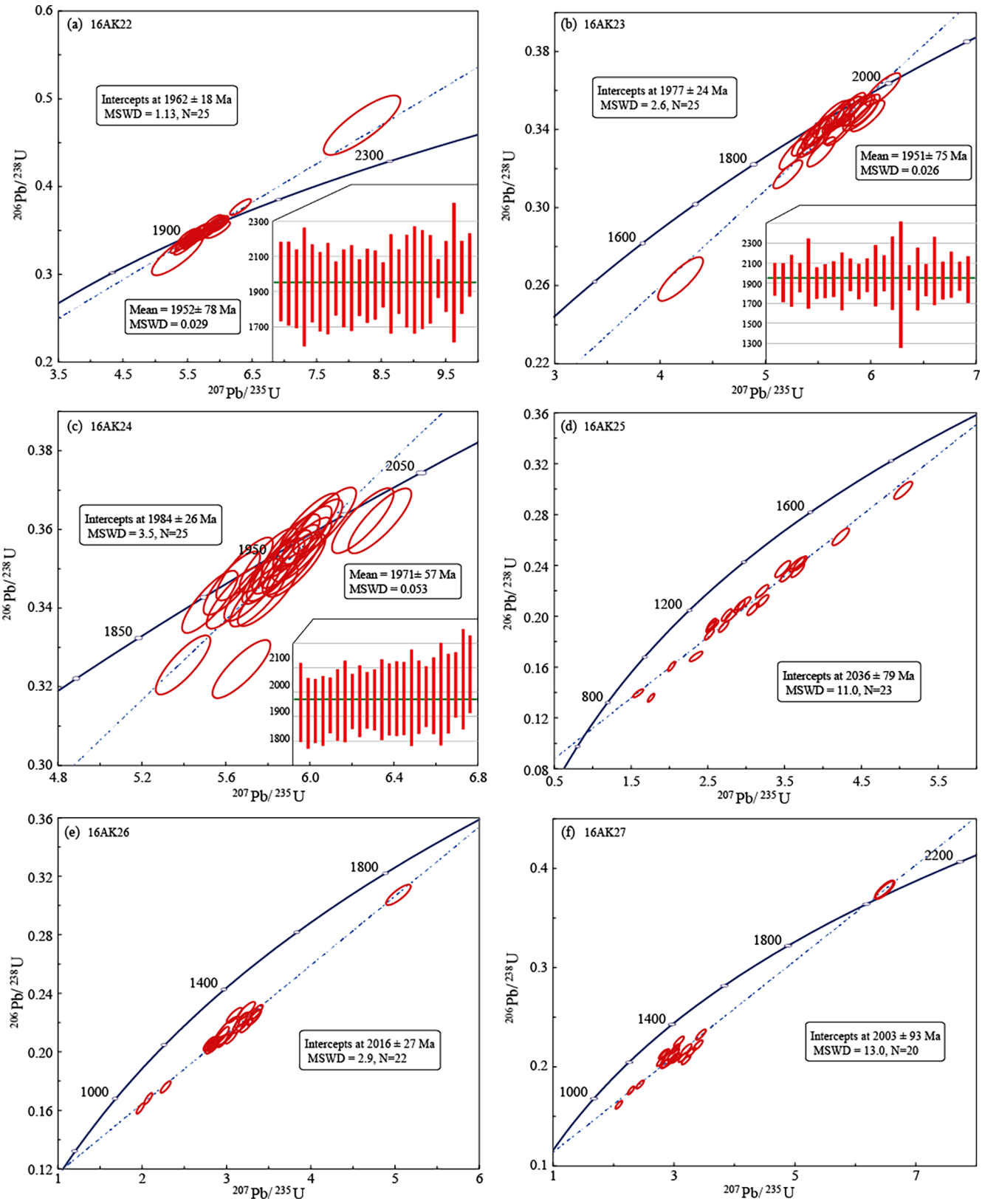


Fig. 8. Zircon U-Pb concordia diagrams and weighted mean $^{206}Pb/^{238}U$ ages of the analyzed samples.

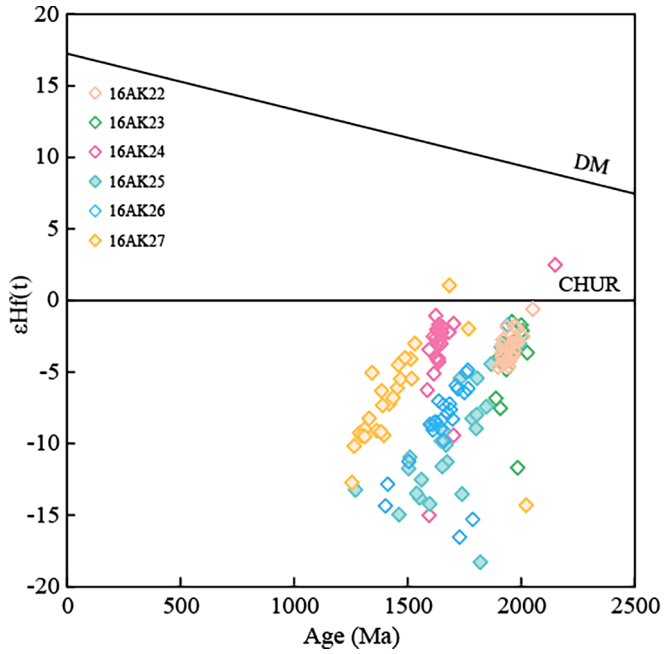


Fig. 9. Diagram of ε_{Hf} (t) values versus ages for zircons in the the granet-biotite gneiss and granulite.

Tarim Craton (Dunhuang Block) is mostly dated as Paleozoic (Zong et al., 2012; He et al., 2014; Wang et al., 2016, 2017a, 217b, 2018), and the Paleoproterozoic metamorphic ages are limited. The available Paleoproterozoic metamorphic age (1.98 Ga) was given by a garnet-sillimanite-quartz schist and a granite gneiss from the Aketashitage area, Dunhuang Block (Lu et al., 2008). Synchronous anatexis events have been reported for the monzonitic granite and igneous carbonate rocks in the same area, which yielded zircon SHRIMP U-Pb anatexic ages of 1.97 Ga and 1.93 Ga, respectively (Xin et al., 2011). Moreover, a simultaneous migmatization event at 2.0 Ga has been recorded by a migmatitic biotite-plagioclase gneiss in the Lapeiquan area (Liu and Wang, 2012). Some other Paleoproterozoic metamorphic ages were reported in the Hongliuxia area, Dunhuang Block (Zhang et al; 2012, 2013a; Zong et al., 2013). In this study, our detailed report about the granulites in the Aketashitage area reveals the existence of Paleoproterozoic high-grade metamorphism in the Dunhuang Block, southeastern margin of the Tarim Craton.

In terms of whole-rock geochemistry characteristics, the Grt-Bi gneisses and mafic granulites display uniform major and trace element compositions. They are strongly peraluminous in composition and have REE patterns that are identical to those from the middle crust but higher than lower continental crust. These data suggest that the Grt-Bi gneisses and mafic granulites share the same source, which is probably the middle continental crust. Although the REE patterns of the garnets from different samples differ considerably, all of them have similarly flat patterns in HREE. Overall, the HREE and Y are relatively low in concentrations, suggesting a garnet-rich source (Otamendi et al., 2002; Carlson, 2012).

Our previous study on the lower-grade meta-felsic and mafic rocks from the Aketashitage area revealed two comparable emplaced ages of 1.96 and 2.06 Ga, and a significant contribution of juvenile materials in the Paleoproterozoic (Wang et al., 2017c). Zircon Hf isotopes of the Grt-Bi gneisses and mafic granulites suggest a long-lived reworking of Archean crust during the Paleoproterozoic. These data demonstrate that the southeastern Tarim Craton simultaneously experienced addition of juvenile material and reworking of preexisting crust in the Paleoproterozoic. The crystallization ages of the meta-felsic and mafic rocks exactly coincide with the metamorphic ages of the Grt-Bi gneisses and mafic granulites, probably indicating a close temporal association of magmatism and metamorphism. Our new data combined with previously published data (Xin et al., 2011, 2012; Long et al., 2014; Wang et al., 2017c) reveal that the southeastern Tarim Craton (Dunhuang Block) is characterized by Paleoproterozoic granulite-facies metamorphism, anatexis and coeval plutonism, which are diagnostic features of active continental margins. In this study, the whole-rock geochemistry and mineral compositions of the analyzed samples suggest that they were possibly formed in the garnet-bearing middle crust, and their granulite-facies metamorphism is probably the consequence of steep subduction. The coeval magmatism and anatexis can be interpreted as a result of the partial melting of the thickening crust related to the collision.

Table 4
Major and trace element compositions for the garnet-biotite gneisses and mafic granulites.

Sample	16AK23	16AK24	16AK26	16AK27
SiO_2	53.2	52.0	54.7	49.3
TiO_2	1.25	1.28	1.1	1.15
$Al2O_3$	17.4	18.1	13.7	14.8
$Fe_2O_3^T$	18.9	19.0	16.7	18.6
MnO	0.20	0.21	0.74	0.71
MgO	4.92	4.96	5.03	6.33
CaO	1.97	1.94	5.22	5.54
Na_2O	1.40	1.48	0.21	0.25
K_2O	1.44	1.66	1.06	1.47
P_2O_5	0.04	0.03	0.33	0.20
Total	99.9	100.0	101.9	101.4
$Mg^{\#}$	37.8	37.8	41.2	44.3
Sc	62	55	45	53
V	310	308	278	342
Cr	237	238	127	132
Co	69	71	58	79
Ni	102	101	81	154
Cu	72	107	18	33
Zn	159	164	173	239
Ga	20	20	20	30
Rb	53.2	59.2	33	45.9
Sr	136	142	118	182
Y	30.2	29.3	36.4	23.7
Zr	96	130	105	99
Nb	6.1	6.6	5.4	5.4
Cs	0.67	0.71	0.49	0.56
Ba	400	500	310	410
La	10	< 10	10	10
Ce	24.7	19.7	30.8	25.8
Pr	3.05	2.35	4.17	3.4
Nd	12.2	9.2	18	14.3
Sm	3.68	3.06	5.22	3.81
Eu	1.16	1.09	1.36	1.33
Gd	5.07	5	7	5.05
Tb	0.92	0.91	1.23	0.91
Dy	5.93	5.76	7.57	5.33
Ho	1.2	1.13	1.46	0.96
Er	3.56	3.52	4.12	2.79
Tm	0.52	0.49	0.58	0.41
Yb	3.4	3.37	3.96	2.63
Lu	0.53	0.49	0.6	0.4
Hf	2.7	3.5	2.9	2.9
Ta	0.4	0.4	0.4	0.4
Pb	8	10	2	2
Th	< 20	< 20	< 20	< 20
U	< 10	< 10	< 10	< 10
A/CNK	2.34	2.33	1.25	1.22
ΣREE	75.9	66.1	96.1	77.1
LREE	54.8	45.4	69.6	58.6
HREE	21.1	20.7	26.5	18.5
LREE/HREE	2.59	2.20	2.62	3.17
La_N/Yb_N	2.11	2.13	1.81	2.73
δEu	0.82	0.85	0.69	0.93
δCe	1.10	1.00	1.17	1.08

Note: $\delta Eu = (Eu_{sample}/Eu_{chondrite})/[(Sm_{sample}/Sm_{chondrite} + Gd_{sample}/Gd_{chondrite})/2]$; $\delta Ce = (Ce_{sample}/Ce_{chondrite})/[(La_{sample}/La_{chondrite} + Pr_{sample}/Pr_{chondrite})/2]$.

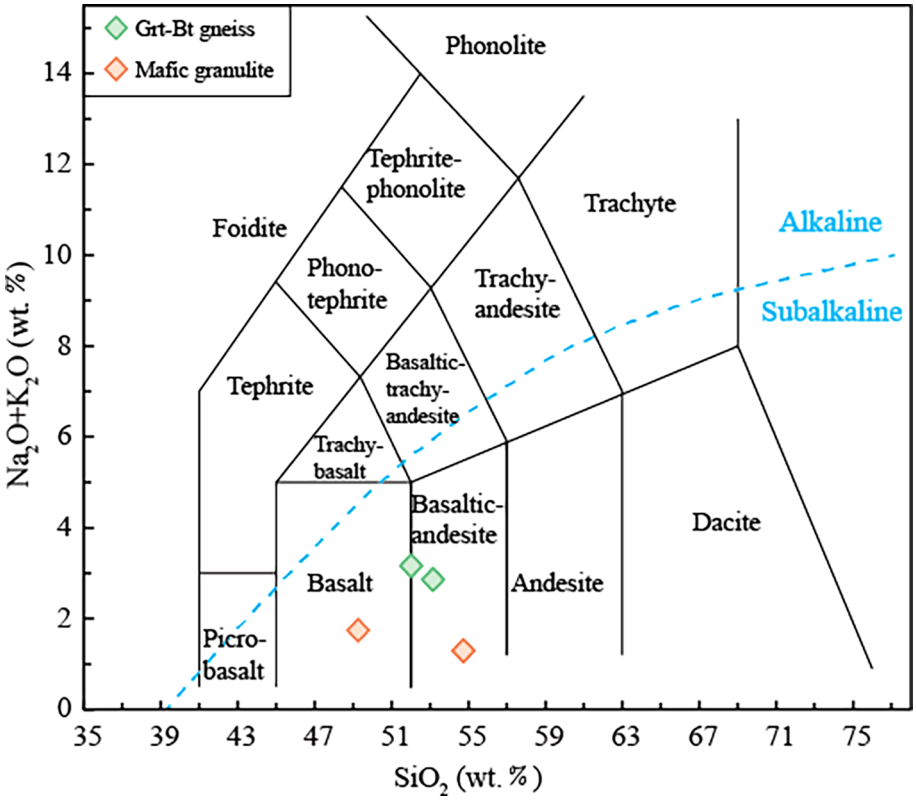


Fig. 10. TAS diagram for the analyzed samples (after Middlemost, 1994).

Based on the aforementioned analysis, we proposed a model (Fig. 12) that the steep subduction of an oceanic lithosphere resulted in the thickening of the continental crust, which in turn caused the crust anatexis. The increase in asthenosphere high heat flow and the intrusion of mantle-derived magma induced extensive heating, which preceded the granulite-facies metamorphism and coeval magmatism in the middle crust of the Dunhuang Block. The long-lived metamorphic processes, revealed by our new data, are possibly the result of continuous subduction. Thus, the Dunhuang Block, located on the southeastern margin of the Tarim Craton, was probably an active continental margin in the Paleoproterozoic, and is considered to be associated with the assembly of the Columbia supercontinent.

9. Conclusions

1. The Grt-Bi gneisses and mafic granulites from the Aketashitage area of the southwest Dunhuang Block yielded metamorphic ages between 1962 and 2036 Ma, which are coeval with the extensive magmatism and anatexis in the same region, indicative of an active continental margin.
2. The Grt-Bi gneisses and mafic granulites have variable but mostly negative ε_{Hf} (t) values of −18.2 to −0.6, fairly uniform Hf isotopic compositions, and highly variable T_{DM}^{C} model ages of 2628 to 3599 Ma, suggesting a long-lived reworking of preexisting crust.
3. The Grt-Bi gneisses and mafic granulites are formed in the garnet-bearing middle crust, and the steep subduction of oceanic slab is probably responsible for their granulite-facies metamorphism.

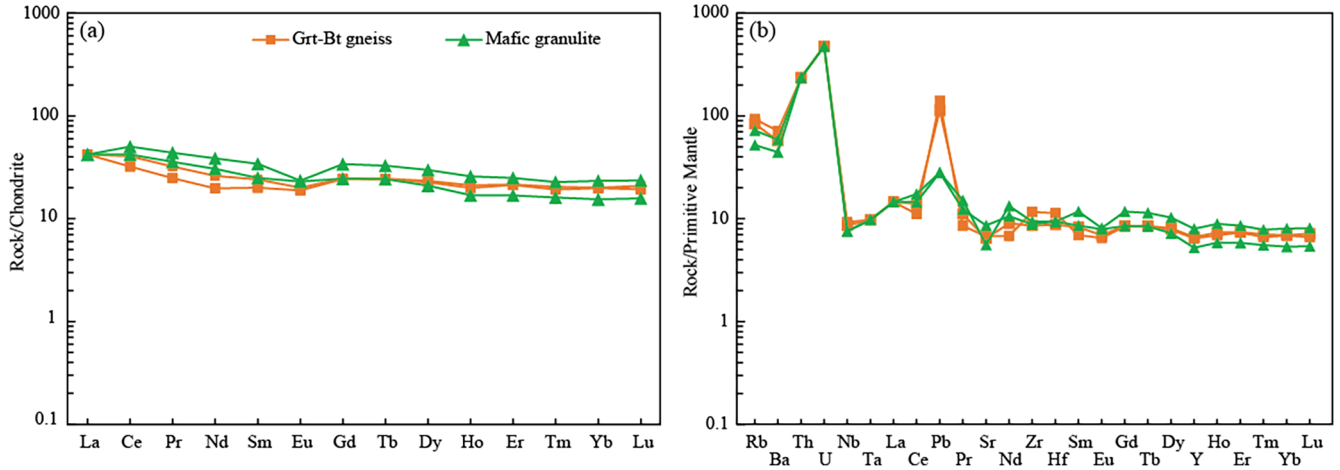


Fig. 11. (a) Chondrite-normalized rare earth element diagrams and (b) primitive mantle-normalized spider diagrams for the analyzed samples. Chondrite- and primitive mantle-normalized values are from Sun and McDonough (1989).

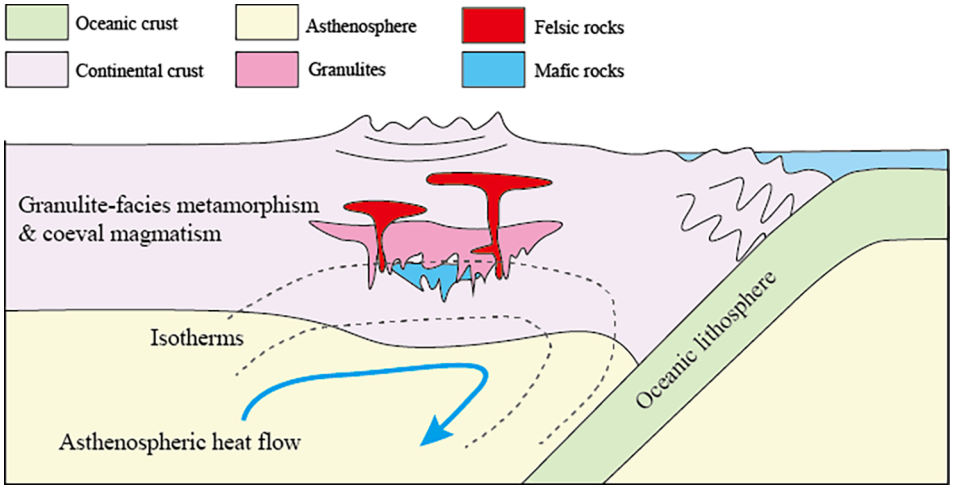


Fig. 12. Schematic model illustrating the tectonic setting of the Dunhuang Block during the Paleoproterozoic.

4. We tentatively proposed that the Dunhuang Block, located on the southeastern margin of the Tarim Craton, was possibly an active continental margin in the Paleoproterozoic, and can be considered to be associated with the assembly of the Columbia supercontinent.

Acknowledgements

This work was financially supported by the National Key R&D Program of China (2017YFC0601205), 973 Program (2014CB440801), National Natural Science Foundation Projects (41702236) and the China Postdoctoral Foundation Fund Project (2015M580133). This paper is a contribution to IGCP 592.

Appendix A. Supplementary data

Supplementary data to this article can be found online at https://doi.org/10.1016/j.precamres.2018.11.003.

References

Bea, F., 1996. Controls on the trace element composition of crustal melts. In: Brown, M., Candela, P.A., Peck, D.L., Stephens, W.E., Walker, R.J., Zen, E.A. (Eds.), The Third Hutton Symposium on the Origin of Granites and Related Rocks. Geological Society of America.

Berman, R.G., Aranovich, L.Ya., Pattison, D.R.M., 1995. Reassessment of the garnet-clinopyroxene Fe-Mg exchange thermometer: II. thermodynamic analysis. Contrib. Miner. Petrol. 119, 30–42.

BGMRG, 1989. Regional geology of Gansu Province, People's Republic of China, Ministry of geology and mineral resources. Geological memoirs, Series 1, No. 19. Geological Publishing House, Beijing (in Chinese).

Bohlen, S., Mezger, K., 1989. Origin of granulite terranes and the formation of the low-ermost continental crust. Science 244 (4902), 326.

Carlson, W.D., 2012. Rates and mechanism of Y, REE, and Cr diffusion in garnet. Am. Mineral. 97 (10), 1598–1618.

Che, Z.C., Sun, Y., 1996. The age of the Altun granulite facies complex and the basement of the Tarim basin. Regional Geology of China 56, 51–57 in Chinese with English abstract.

Collins, W.J., 2002. Nature of extensional accretionary orogens. Tectonics 21 (4), 6-1-6-12.

Condie, K.C., 2002. Breakup of a Paleoproterozoic Supercontinent. Gondwana Res. 5 (1), 41–43.

Debari, S.M., 1994. Petrogenesis of the Fiambalá Gabbroic Intrusion, Northwestern Argentina, a Deep Crustal Syntectonic Pluton in a Continental Magmatic Arc. J. Petrol. 35 (3), 679–713.

Ge, R., Zhu, W., Wu, H., Zheng, B., He, J., 2013b. Timing and mechanisms of multiple episodes of migmatization in the Korla Complex, northern Tarim Craton, NW China: Constraints from zircon U-Pb-Lu-Hf isotopes and implications for crustal growth. Precambr. Res. 231, 136–156.

Ge, R., Zhu, W., Wu, H., He, J., Zheng, B., 2013a. Zircon U-Pb ages and Lu-Hf isotopes of Paleoproterozoic metasedimentary rocks in the Korla Complex, NW China: Implications for metamorphic zircon formation and geological evolution of the Tarim Craton. Precambr. Res. 231, 1–18.

Ge, R., Zhu, W., Wilde, S.A., He, J., Cui, X., 2015. Synchronous crustal growth and reworking recorded in late Paleoproterozoic granitoids in the northern Tarim craton: in situ zircon U-Pb-Hf-O isotopic and geochemical constraints and tectonic implications. Geol. Soc. Am. Bull. 127 (5–6), 781–803.

Ge, R., Zhu, W., Wilde, S.A., Wu, H., 2018. Remnants of Eoarchean continental crust derived from a subducted proto-arc. Sci. Adv. 4 (2).

Glebovitsky, V.A., Nikitina, L.P., Khiltova, V.Ya., Ovchinnikov, N.O., 2004. The thermal regimes of the upper mantle beneath Precambrian and Phanerozoic structures up to the thermobarometry data of mantle xenoliths. Lithos 74, 1–20.

Harley, S., 1989. The origins of granulites: a metamorphic perspective. Geol. Mag. 126 (3), 215–247.

Harley, S.L., Kelly, N.M., Möller, A., 2007. Zircon behaviour and the thermal histories of mountain chains. Elements 3 (1), 25–30.

He, Z.Y., Zhang, Z.M., Zong, K.Q., Dong, X., 2013. Paleoproterozoic crustal evolution of the Tarim Craton: constrained by zircon U-Pb and Hf isotopes of meta-igneous rocks from Korla and Dunhuang. J. Asian Earth Sci. 78, 54–70.

He, Z., Zhang, Z., Zong, K., Xiang, H., Klemd, R., 2014. Metamorphic P-T-t evolution of mafic HP granulites in the northeastern segment of the Tarim Craton (Dunhuang block): evidence for early Paleozoic continental subduction. Lithos 196–197, 1–13.

Hickmott, D.D., Shimizu, N., 1990. Trace element zoning in garnet from the Kwoiek Area, British Columbia: disequilibrium partitioning during garnet growth? Contrib. Miner. Petrol. 104 (6), 619–630.

Hickmott, D., Spear, F.S., 1992. Major-and trace-element zoning in garnets from calcar-eous pelites in the NW Shelburne Falls Quadrangle, Massachusetts: garnet growth histories in retrograded rocks. J. Petrol. 33 (5), 965–1005.

Holdaway, M.J., 2000. Application of new experimental and garnet Margules data to the garnet-biotite geothermometer. Am. Mineral. 85, 881–892.

Hoskin, P.W.O., Black, L.P., 2000. Metamorphic zircon formation by solid-state re-crystallization of protolith igneous zircon. J. Metamorph. Geol. 18 (4), 423–439.

Hoskin, P.W., Schaltegger, U., 2003. The composition of zircon and igneous and meta-morphic petrogenesis. Rev. Mineral. Geochem. 53 (1), 27–62.

Hu, Z., Zhang, W., Liu, Y., Gao, S., Li, M., Zong, K., Chen, H., Hu, S., 2014. "Wave" signal-smoothing and mercury-removing device for laser ablation quadrupole and multiple collector ICPMS analysis: application to lead isotope analysis. Anal. Chem. 87 (2), 1152–1157.

Hyndman, R.D., Currie, C.A., Mazzotti, S.P., 2005. Subduction zone backarcs, mobile belts, and orogenic heat. GSA Today 15 (2), 4–10.

Jagoutz, O., Müntener, O., Ulmer, P., Pettke, T., Burg, J.P., Dawood, H., Hussain, S., 2007. Petrology and mineral chemistry of lower crustal intrusions: the Chilas Complex, Kohistan (NW Pakistan). J. Petrol. 48 (10), 1895–1953.

Kelly, N.M., Harley, S.L., 2005. An integrated microtextural and chemical approach to zircon geochronology: refining the Archaean history of the Napier Complex, east Antarctica. Contrib. Miner. Petrol. 149 (1), 57–84.

Klepeis, K.A., King, D.M., Paoli, De, Clarke, G.L., Gehrels, G., 2007. Interaction of strong lower and weak middle crust during lithospheric extension in western New Zealand. Tectonics 26, (4).

Kohn, M.J., Spear, F., 2000. Retrograde net transfer reaction insurance for pressure-temperature estimates. Geology 28 (12), 1127–1130.

Li, Q.L., Li, X.H., Liu, Y., Tang, G.Q., Yang, J.H., Zhu, W.G., 2010. Precise U-Pb and Pb-Pb dating of Phanerozoic baddeleyite by SIMS with oxygen flooding technique. J. Anal. At. Spectrom. 25 (7), 1107–1113.

Li, X.H., Liu, Y., Li, Q.L., Guo, C.H., Chamberlain, K.R., 2009. Precise determination of Phanerozoic zircon Pb/Pb age by multicollector SIMS without external standardiza-tion. Geochem. Geophys. Geosyst. 10 (4), 1–21.

Liu, Y., Hu, Z., Gao, S., Günther, D., Xu, J., Gao, C., Chen, H., 2008. In situ analysis of major and trace elements of anhydrous minerals by LA-ICP-MS without applying an internal standard. Chem. Geol. 257 (1), 34–43.

Liu, H., Wang, G.C., 2012. LA-ICP-MS zircon U-Pb dating of gneiss of Milan Group and mafic dyke swarms from Lapeiquan in northern Altun and its tectonic significance. Geological Bulletin of China 31, 1461–1468 in Chinese with English abstract.

Liu, Y.S., Yu, H.F., Xin, H.T., Lu, S.N., Xiu, Q.Y., Li, Q., 2009. Tectonic units division and

Precambrian significant geological events in Altyn Tagh Mountain, China. Geol. Bull. China 28, 1430–1438 in Chinese with English abstract.
Long, X., Yuan, C., Sun, M., Xiao, W., Zhao, G., Zhou, K., Wang, Y., Hu, A., 2011. The discovery of the oldest rocks in the Kuluketage area and its geological implications. Sci. China Earth Sci. 54 (3), 342–348.
Long, X., Yuan, C., Sun, M., Kröner, A., Zhao, G., 2014. New geochemical and combined zircon U-Pb and Lu-Hf isotopic data of orthogneisses in the northern Altyn Tagh, northern margin of the Tibetan plateau: implication for Archean evolution of the Dunhuang Block and crust formation in NW China. Lithos 200–201, 418–431.
Long, X., Wilde, S.A., Yuan, C., Hu, A., Sun, M., 2015. Provenance and depositional age of Paleoproterozoic metasedimentary rocks in the Kuluketage Block, northern Tarim Craton: implications for tectonic setting and crustal growth. Precambr. Res. 260, 76–90.
Lu, S.N., 2002b. A review of major problems of Precambrian research. Prog. Precambr. Res. 25, 65–72 in Chinese with English abstract.
Lu, S.N., 2002a. In: Preliminary study of Precambrian geology in Tibet-Qinghai plateau. Geology publishing house, pp. 135 in Chinese.
Lu, S., Li, H., Zhang, C., Niu, G., 2008. Geological and geochronological evidence for the Precambrian evolution of the Tarim Craton and surrounding continental fragments. Precambr. Res. 160 (1–2), 94–107.
Lu, S.N., Yu, H.F., Li, H.M., Guo, K.Y., Wang, H.K., Jin, W., Zhang, C.L., Liu, Y.S., 2006a. In: Research on Precambrian Major Problems in China. Geological Publishing Press, Beijing, pp. 1–206 in Chinese.
Lu, S., Yu, H., Li, H., Guo, K., Wang, H., Jin, W., Zhang, C., Liu, Y., 2006b. In: Research on Precambrian Major Problems in China. Geological Publishing Press, Beijing, pp. 206 in Chinese.
Lu, S.N., Yuan, G.B., 2003. Geochronology of early Precambrian magmatic activeties in Aketashitage, East Altyn Tagh. Acta Geol. Sin. 77, 61–68 in Chinese with English abstract.
Ludwig, K., 2003. In: Isoplot 3.0, a geochronological toolkit for Microsoft Excel. Berkeley Geochronological Centre Special Publication No. 4, pp. 71 edited.
Mao, X., Zhang, J., Yu, S., Li, Y., Yu, X., Lu, Z., 2017. Early Paleozoic granulite-facies metamorphism and anatexis in the northern West Qinling orogen: monazite and zircon U-Pb geochronological constraints. Sci. China Earth Sci. 60 (5), 943–957.
Mei, H.L., Yu, H.F., Li, Q., Zuo, G.C., 1997. Preliminary litho-tectonic framework of early precambrian rocks in Dunhuang-Beishan area, Gansu, West China. Prog. Precambr. Res. 20, 47–54 in Chinese with English abstract.
Mei, H.L., Yu, H.F., Lu, S.N., Li, H.M., Li, Q., Lin, Y.X., Zuo, G.C., 1998. Archean tonalite in the Dunhuang, Gansu province: age from U-Pb single zircon and Nd isotope. Prog. Precambr. Res. 21, 41–45 in Chinese with English abstract.
Michael, B., 2007. Metamorphism, Plate Tectonics, and the Supercontinent Cycle. Earth Sci. Front. 14 (1), 1–18.
Middlemost, E.A.K., 1994. Naming materials in the magma/igneous rock system. Earth Sci. Rev. 37, 215–224.
MÜNtener, O., Hermann, J., Trommsdorff, V., 2000. Cooling history and exhumation of lower-crustal granulite and upper mantle (Malenco, Eastern Central Alps). J. Petrol. 41 (2), 175–200.
Otamendi, J.E., Jesús, D., Douce, A.E.P., Castro, A., 2002. Rayleigh fractionation of heavy rare earths and yttrium during metamorphic garnet growth. Geology 30 (2), 159–162.
Rogers, J.J.W., Santosh, M., 2002. Configuration of Columbia, a Mesoproterozoic Supercontinent. Gondwana Res. 5 (1), 5–22.
Rogers, J.J.W., Santosh, M., 2003. Supercontinents in Earth History. Gondwana Res. 6 (3), 357–368.
Rubatto, D., 2002. Zircon trace element geochemistry: partitioning with garnet and the link between U-Pb ages and metamorphism. Chem. Geol. 184 (1), 123–138.
Rudnick, R.L., Fountain, D.M., 1995. Nature and composition of the continental crust: a lower crustal perspective. Rev. Geophys. 33 (3), 267–309.
Rudnick, R.L., Gao, S., 2003. 3.01 – Composition of the Continental Crust A2 – Holland, Heinrich D. In: Turekian, K.K. (Ed.), Treatise on Geochemistry. Pergamon, Oxford, pp. 1–64.
Stacey, J.S., Kramers, J.D., 1975. Approximation of terrestrial lead isotope evolution by a two-stage model. Earth Planet. Sci. Lett. 26 (2), 207–221.
Sun, S.S., McDonough, W.F., 1989. Chemical and isotopic systematics of oceanic basalts: implications for mantle composition and processes. Geol. Soc. London Spec. Publ. 42, 313–345.
Vavra, G., Schmid, R., Gebauer, D., 1999. Internal morphology, habit and U-Th-Pb microanalysis of amphibolite-to-granulite facies zircons: geochronology of the Ivrea Zone (Southern Alps). Contrib. Miner. Petrol. 134 (4), 380–404.
Villaseca, C., Downes, H., Pin, C., Barbero, L., 1999. Nature and composition of the lower continental crust in Central Spain and the Granulite-Granite Linkage: inferences from Granulitic Xenoliths. J. Petrol. 40 (10), 1465–1496.
Wang, H., Chen, H.X., Lu, J.S., Wang, G.D., Peng, T., Zhang, H., Yan, Q.R., Hou, Q.L., Zhang, Q., Wu, C.M., 2016. Metamorphic evolution and SIMS U-Pb geochronology of the Qingshigou area, Dunhuang block, NW China: tectonic implications of the southernmost Central Asian orogenic belt. Lithosphere 8 (5), 463–479.
Wang, H.Y.C., Chen, H.X., Zhang, Q.W.L., Shi, M.Y., Yan, Q.R., Hou, Q.L., Zhang, Q., Kusky, T., Wu, C.M., 2017a. Tectonic mélange records the Silurian-Devonian subduction-metamorphic process of the southern Dunhuang terrane, southernmost Central Asian Orogenic Belt. Geology 45 (5), 427–430.
Wang, Z.M., Han, C.M., Su, B.X., Sakyi, P.A., Malaviarachchi, S.P.K., Ao, S.J., Wang, L.J., 2013. The metasedimentary rocks from the eastern margin of the Tarim Craton: petrology, geochemistry, zircon U-Pb dating, Hf isotopes and tectonic implications. Lithos 179, 120–136.
Wang, Z.M., Han, C.M., Xiao, W.J., Wan, B., Sakyi, P.A., Ao, S.J., Zhang, J.E., Song, D.F., 2014. Petrology and geochronology of Paleoproterozoic garnet-bearing amphibolites from the Dunhuang Block, Eastern Tarim Craton. Precambr. Res. 255 163–180.
Wang, Z.M., Han, C.M., Xiao, W.J., Su, B.X., Ding, J.X., 2017c. Paleoproterozoic subduction-related magmatism and crustal evolution of the Dunhuang Block, NW China. J. Asian Earth Sci. 134, 13–28.
Wang, Z.M., Han, C.M., Xiao, W.J., Su, B.X., Ding, J.X., Song, S.H., 2017d. Geochemical and zircon U-Pb and Lu-Hf isotopic constraints on the origin of supracrustal rocks from the mid-Qilian terrane: a comparison between supracrustal rocks on the two sides of the eastern segment of the Altyn Tagh Fault. Precambr. Res. 294, 284–306.
Wang, Z.M., Han, C.M., Xiao, W.J., Wan, B., Sakyi, P.A., 2017e. Paleozoic subduction-related magmatism in the Duobagou area, Dunhuang block: constrained by zircon U-Pb geochronology and Lu-Hf isotopes and whole-rock geochemistry of metaigneous rocks. Lithosphere 9 (6), 1012–1032.
Wang, H.Y.C., Wang, J., Wang, G.D., Lu, J.S., Chen, H.X., Peng, T., Zhang, H.C.G., Zhang, Q.W.L., Xiao, W.J., Hou, Q.L., Yan, Q.R., Zhang, Q., Wu, C.M., 2017b. Metamorphic evolution and geochronology of the Dunhuang orogenic belt in the Hongliuxia area, northwestern China. J. Asian Earth Sci. 135, 51–69.
Wang, H.Y., Zhang, Q.W.H., Chen, X., Liu, J.H., Zhang, H.C., Pham, V.T., Peng, T., Wu, C.M., 2018. Paleozoic subduction of the southern Dunhuang Orogenic Belt, northwest China: metamorphism and geochronology of the Shuixiakou area. Geodin. Acta 30 (1), 63–83.
Wei, C.J., 2016. Granulite facies metamorphism and petrogenesis of granite (II): quantitative modeling of the HT-UHT phase equilibria for metapelites and the petrogenesis of S-type granite. Acta Petrol. Sin. 32 (6), 1625–1643 in Chinese with English abstract.
Wu, F.Y., Yang, Y.H., Xie, L.W., Yang, J.H., Xu, P., 2006. Hf isotopic compositions of the standard zircons and baddeleyites used in U-Pb geochronology. Chem. Geol. 234 (1–2), 105–126.
Xiang, H., Zhang, Z.M., Lei, H.C., Qi, M., Dong, X., Wang, W., Lin, Y.H., 2014. Paleoproterozoic ultrahigh-temperature pelitic granulites in the northern Sulu orogen: constraints from petrology and geochronology. Precambr. Res. 254, 273–289.
Xiao, W.J., Mao, Q.G., Windley, B.F., Han, C.M., Qu, J.F., Zhang, J.E., Ao, S.J., Guo, Q.Q., Cleven, N.R., Lin, S.F., Shan, Y.H., Li, J.L., 2010. Paleozoic multiple accretionary and collisional processes of the Beishan orogenic collage. Am. J. Sci. 310, 1553–1594.
Xie, L., Zhang, Y., Zhang, H., Sun, J., Wu, F., 2008. In situ simultaneous determination of trace elements, U-Pb and Lu-Hf isotopes in zircon and baddeleyite. Chin. Sci. Bull. 53 (10), 1565–1573.
Xin, H.T., Liu, Y.S., Luo, Z.H., Song, S.C., Wang, S.Q., 2013. The growth of Archean continental crust in Aqtashtagh area of southeast Tarim, China: constraints from petrochemistry and chronology about Milan Group and TTG-gneiss. Earth Sci. Front. 20, 240–259 in Chinese with English abstract.
Xin, H.Y., Luo, Z.H., Liu, Y.S., Wang, S.Q., Zhang, Z.L., 2012. Geological features and significance of Paleoproterozoic carbonatite of crustal origin in Aqtashtagh area of southeast Tarim Basin, China. Earth Sci. Front. 19, 167–178 in Chinese with English abstract.
Xin, H.T., Zhao, F.Q., Luo, Z.H., Liu, Y.S., Wan, Y.S., Wang, S.Q., 2011. Determination of the Paleoproterozoic geochronological framework in Aqtashtagh area in southeastern Tarim, China. Acta Geol. Sin. 85, 1977–1993 in Chinese with English abstract.
Xu, Z.Q., Yang, J.S., Zhang, J.X., Jiang, M., Li, H.B., Cui, J.W., 1999. A comparison between the tectonic units on the two sides of the Altun sinistral strike-slip fault and the mechanism of lithospheric shearing. Acta Geol. Sin. 73, 193–205 in Chinese with English abstract.
Xu, Z.Q., Li, S.T., Zhang, J.X., Yang, J.S., He, B.Z., Li, H.B., Lin, C.S., Cai, Z.H., 2011. PaleoAsian and Tethyan tectonic systems with docking the Tarim block. Acta Petrol. Sin. 27, 1–22 in Chinese with English abstract.
Xu, Z.Q., He, B.Z., Zhang, C.L., Zhang, J.X., Wang, Z.M., Cai, Z.H., 2013. Tectonic framework and crustal evolution of the Precambrian basement of the Tarim Block in NW China: New geochronological evidence from deep drilling samples. Precambr. Res. 235, 150–162.
Yang, J.H., Wu, F.Y., Shao, J.A., Wilde, S.A., Xie, L.W., Liu, X.M., 2006. Constraints on the timing of uplift of the Yanshan Fold and Thrust Belt, North China. Earth Planet. Sci. Lett. 246 (3–4), 336–352.
Yu, H., Mei, H., Li, Q., 1998. The characteristics of Archean khondalite series in Dunhuang, Gansu province. Prog. Precambr. Res. 01, 19–25 in Chinese with English abstract.
Zhang, Z., Dong, X., Xiang, H., Liou, J.G., Santosh, M., 2013b. Building of the Deep Gangdese Arc, South Tibet: paleocene Plutonism and Granulite-Facies metamorphism. J. Petrol. 54 (12), 2547–2580.
Zhang, J.X., Gong, J.H., Yu, S.Y., 2012. 1.85 Ga HP granulite-facies metamorphism in the Dunhuang block of the Tarim Craton, NW China: evidence from U-Pb zircon dating of mafic granulites. J. Geol. Soc. 169, 511–514.
Zhang, J., Li, H., Meng, F., Xiang, Z., Yu, S., Li, J., 2011. Polyphase tectonothermal events recorded in"metamorphic basement"from the Altyn Tagh, the southeastern margin of the Tarim basin, western China: constraint from U-Pb zircon geochronology. Acta Petrol. Sin. 27 (1), 24 in Chinese with English abstract.
Zhang, J., Yu, S., Gong, J., Li, H., Hou, K., 2013a. The latest Neoarchean-Paleoproterozoic evolution of the Dunhuang block, eastern Tarim craton, northwestern China: Evidence from zircon U-Pb dating and Hf isotopic analyses. Precambr. Res. 226, 21–42.
Zhao, G., Cawood, P.A., 2012. Precambrian geology of China. Precambr. Res. 222–223, 13–54.
Zhao, G., Cawood, P.A., Wilde, S.A., Sun, M., 2002. Review of global 2.1-1.8 Ga orogens: implications for a pre-Rodinia supercontinent. Earth Sci. Rev. 59 (1–4), 125–162.
Zhao, Y., Diwu, C., Sun, Y., Zhu, T., Wang, H., 2013. Zircon geochronology and Lu-Hf isotope compositions for Precambrian rocks of the Dunhuang complex in Shuixiakou area, Gansu Province. Acta Petrol. Sin. 29 (5), 1698–1712 in Chinese with English

abstract.
Zhao, Y., Diwu, C., Zhu, T., Wang, H., Sun, Y., 2015a. Discovery of the Late Devonian plagiogranite in Sanweishan area, Dunhuang, Gansu province and its geological implications. Acta Petrol. Sin. 31, 1855–1869 in Chinese with English abstract.
Zhao, G., Sun, M., Wilde, S.A., Li, S., 2004. A Paleo-Mesoproterozoic supercontinent: assembly, growth and breakup. Earth Sci. Rev. 67 (1–2), 91–123.
Zhao, Y., Sun, Y., Yan, J., Diwu, C., 2015b. The Archean-Paleoproterozoic crustal evolution in the Dunhuang region, NW China: constraints from zircon U-Pb geochronology and in situ Hf isotopes. Precambr. Res. 271, 83–97.
Zhao, Y., Sun, Y., Diwu, C., Guo, A.L., Ao, W.H., Zhu, T., 2016. The Dunhuang block is a Paleozoic orogenic belt and part of the Central Asian Orogenic Belt (CAOB), NW China. Gondwana Res. 30, 207–223.
Zhao, Y., Sun, Y., Diwu, C., Zhu, T., Ao, W., Zhang, H., Yan, J., 2017. Paleozoic intrusive rocks from the Dunhuang tectonic belt, NW China: constraints on the tectonic evolution of the southernmost Central Asian Orogenic Belt. J. Asian Earth Sci. 138, 562–587.
Zong, K., Liu, Y., Zhang, Z., He, Z., Hu, Z., Guo, J., Chen, K., 2013. The generation and evolution of Archean continental crust in the Dunhuang block, northeastern Tarim craton, northwestern China. Precambr. Res. 235, 251–263.
Zong, K., Klemd, R., Yuan, Y., He, Z., Guo, J., Shi, X., Liu, Y., Hu, Z., Zhang, Z., 2017. The assembly of Rodinia: The correlation of early Neoproterozoic (ca. 900Ma) high-grade metamorphism and continental arc formation in the southern Beishan Orogen southern Central Asian Orogenic Belt (CAOB). Precambr. Res. 290, 32–48.
Zong, K.Q., Zhang, Z.M., He, Z.Y., Hu, Z.C., Santosh, M., Liu, Y.S., Wang, W., 2012. Early Palaeozoic high-pressure granulites from the Dunhuang block, northeastern Tarim Craton: constraints on continental collision in the southern Central Asian Orogenic Belt. J. Metamorph. Geol. 30 (8), 753–768.